Mechanical Compaction

Beatriz Menendez, Teng-Fong Wong, Christian David

Chapter 2 ►

Mechanical Compaction

Teng-fong Wong
Christian David
Beatriz Menéndez

2.1 Introduction

In response to an applied stress field or pore pressure changes, the pore space of a rock may compact or dilate. Mechanical compaction induces the porosity to decrease, and as a physical mechanism of diagenesis it can play an important role, especially during early and intermediate burial (Pettijohn, 1975; Berner, 1980; Choquette and James, 1986). At depths greater than 4.5 km or so the conventional thinking is that chemical compaction processes such as pressure solution (Chapter 3) dominates, and yet recent observations indicate that mechanical compaction may persist to these depths in deeply buried sandstones (Schutjens and de Ruig, 1997; Fisher et al., 1999). In active tectonic settings such as accretionary prisms (Bray and Karig, 1985; Byrne et al., 1983) and fault zones (Byerlee, 1990; Sibson, 1994), mechanical compaction can influence the development of porosity loss, dewatering, and pore pressure excess.

Mechanical compaction is central to many problems in reservoir and geotechnical engineering, for which deformation and fluid transport are intimately related. The extraction of hydrocarbon and groundwater reduces pore pressure and thus causes an increase in the effective stress in a reservoir and aquifer. For very porous or weakly consolidated formations, the increase in effective stress may be sufficient to cause inelastic deformation (Smits et al., 1988; Jones and Leddra, 1989; Zhang et al., 1990a; Wong et al., 1997), and modify the stress field (Teufel et al., 1991; Segall and Fitzgerald, 1998) as well as hydromechanical properties (Goldsmith, 1989; Rhett and Teufel, 1992; David et al., 1994; Zhu and Wong, 1997; Schutjens and de Ruig, 1997).

In response to groundwater withdrawal and reservoir depletion, the compactive deformation and failure may be spatially extensive or localized to the vicinity of the wellbore, but in either case the consequences can be economically severe,

involving surface subsidence (Boutéca et al., 1996; Nagel, 2001), induced seismicity (Segall, 1989; Grasso and Wittlinger, 1990; Doser et al., 1991), well failure (Fredrich et al., 2000), and various production problems. Knowledge of the compactive response of rock masses to stress is also relevant to other environmental and geotechnical applications, including drilling technology (Thiercelin, 1989; Suarez-Rivera et al., 1990), nuclear waste isolation (e.g., Davis, 1991), tunnel settlement (Jeng et al., 2002), and terrestrial sequestration of carbon dioxide (Wawersik et al., 2000).

In these geological and geotechnical applications the ability to predict the occurrence and extent of deformation and failure hinges upon a fundamental understanding of the phenomenology and micromechanics of compaction. This chapter reviews recent advances in rock mechanics research on the mechanical compaction of porous rocks, focusing on a number of specific questions. Our review will emphasize the synthesis of laboratory data, quantitative characterization of damage, and theoretical models.

Traditionally the compaction and subsidence of aquifers and reservoirs are analyzed by a poroelastic model, with the mechanical response characterized by an elastic modulus such as compressibility. What are the appropriate values for the rock compressibility, and to what extent can inelastic deformation be neglected? Field studies and microstructural observations have shown that inelastic deformation, pore collapse, and grain crushing may be pervasive in certain settings. How can laboratory studies conducted under controlled conditions provide insights into the phenomenology of inelastic and compactive failure and constraints on the constitutive models? To relate the laboratory data to diagenetic and reservoir settings it is necessary to extrapolate in spatial and temporal scales. Microstructural observations on naturally and experimentally deformed samples can establish linkage on the deformation and failure mechanisms, and significant advances have been made in the quantitative and three-dimensional imaging of damage in geomaterials. How is the damage evolution related to the micromechanics of compaction? How do constitutive parameters in elastic-plastic models scale with microstructural parameters such as grain size and porosity?

We will adopt the convention that compressive stresses and compactive strains (i.e., shortening and porosity decrease) are positive, and we denote the maximum and minimum (compressive) principal stresses by σ_1 and σ_3, respectively. The pore pressure will be denoted by p, and the difference between the confining pressure P_c and pore pressure will be referred to as the effective pressure P_e.

2.2 Phenomenology of Mechanical Compaction in Porous Rocks

2.2.1 Linear and Nonlinear Elastic Behavior

Traditionally, compaction in reservoirs and aquifers is analyzed using poroelasticity. Terzaghi's one-dimensional consolidation theory is commonly used in soil

mechanics (Lambe and Whitman, 1969) and hydrology (Domenico and Schwartz, 1998). A more general theory was formulated by Biot (1941), and in reservoir mechanics the model formulated by Geertsma (1973) is adopted in many practical applications. In Geertsma's compaction model the key mechanical parameter is the uniaxial compressibility β_1, defined to be the relative change in axial length per unit change in pore pressure in an oedometer test on a cylindrical sample with radial strain maintained at zero. For a disk-shaped reservoir (with thickness h and radius R) located horizontally at a depth c below the free surface of a formation, Geertsma (1973) derived that a change in pore pressure Δp in the reservoir would induce a surface subsidence (at a radial distance r from the center of the disk) of the amount $2Ah(1-\nu)\beta_1\Delta p$, where A is a geometric factor dependent on the ratios r/R and c/R. Hence the oedometer measurements can conveniently be used to relate reservoir depletion to surface subsidence.

Geertsma's (1973) compilation and other oedometer measurements (Brace and Riley, 1972; Smits et al., 1988; Schutjens and de Ruig, 1997) of uniaxial compressibility values underscore several important features of poroelastic behavior in porous rocks.

- It is sensitively dependent on porosity and degree of lithification. At effective vertical stresses of 30–60 MPa, the β_1 values of well-consolidated sandstones (with porosities of 3% to 20%) fall in the range of $0.2 - 2.0 \times 10^{-4}$ MPa^{-1}, whereas those for unconsolidated sandstones (with porosities of 30% to 40%) fall in the range of $5 - 20 \times 10^{-4}$ MPa^{-1}. In chalk with porosity more than 35% or so, β_1 is on the order of 1×10^{-3} MPa^{-1}.
- The compressibility varies significantly with lithology and, in general, sandstones are more compressible than carbonate rocks. At an effective vertical stress of 30–60 MPa, the uniaxial compressibility of a well-consolidated limestone (with porosity up to 20%) falls in the range of $0.1 - 0.5 \times 10^{-4}$ MPa^{-1}.
- The compressibility behavior is nonlinear with the β_1 value strongly stress dependent.

Extensive measurement of the bulk compressibility β under hydrostatic stress condition has also been made. From poroelasticity theory it can be shown that the two compressibilities are related by

$$\beta_1 = \frac{b}{3}\frac{(1+\nu)}{(1-\nu)}\beta = \frac{b}{3}\frac{(1+\nu)}{(1-\nu)}\frac{1}{K}, \tag{2.1}$$

where ν is the Poisson ratio, K is the drained bulk modulus, and b is the Biot coefficient (Chapter 1). For $0 \leq \nu \leq 0.5$ the ratio β_1/β ranges from $b/3$ to b, and since $b \leq 1$ the uniaxial compressibility from an oedometer test is less than the bulk compressibility measured in a hydrostatic test. Sandstone data of Schutjens and de Ruig (1997) are in agreement with this inequality at relatively low effective stresses.

Because the applied stress is uniform in a hydrostatic test, interpretation of the compressibility behavior is not as complicated as that in an oedometer test involving mixed boundary conditions. The effects of porosity and effective pressure on sandstone compressibility are illustrated in Figure 2.1 from Zimmerman (1991), who calculated the bulk compressibility from Fatt's (1958) pore compressibility data for 14 sandstones with porosities ranging from 9% to 24%. The high and low values correspond to the compressibility at effective pressures of 0 and 103.5 MPa, respectively. We also include the data of Zhang et al. (1990b) for a Boise sandstone sample with 35% porosity. The low value for this case corresponds to an effective pressure of 50 MPa.

There is an approximate trend for the compressibility to increase with porosity, but certainly no simple correlation between the two parameters. The lack of a clear trend is probably because the appreciable decrease of compressibility with pressure in this regime arises from elastic closure of microcracks that constitute only a small subset of the total porosity. Increasing the effective pressure up to 100 MPa or so induces the progressive closure of microcracks in the sandstones, which is manifested by a decrease in compressibility (Walsh, 1965).

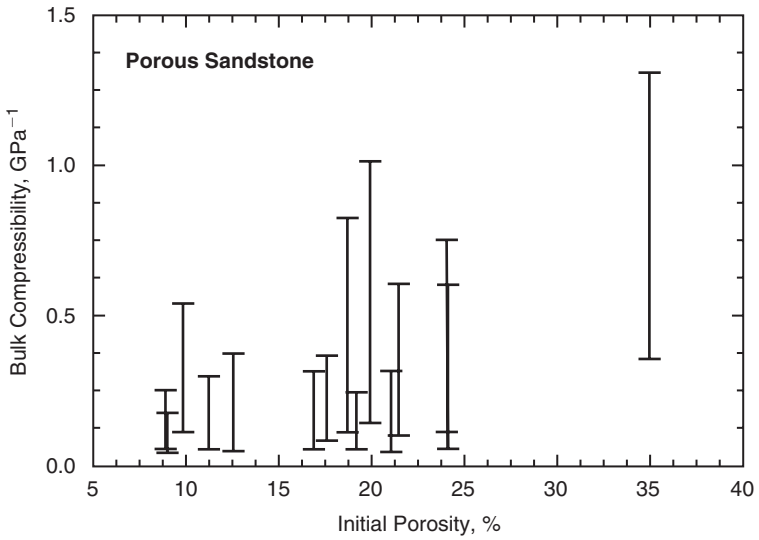

Figure 2.1 ► Compressibility of sandstone as function of porosity at two different effective pressures. Fatt's (1958) data for 14 sandstones with porosities ranging from 9% to 24.1% were compiled by Zimmerman (1991) in his Table 3.1. The high and low values correspond to measurements at effective pressures of 0 and 103.5 MPa, respectively. The data for the Boise sandstone with 35% porosity were reported by Zhang et al. (1990b). The high and low values correspond to measurements at effective pressures of 3 and 50 MPa, respectively.

A number of empirical relations have been proposed for compressibility as a function of effective pressure in this regime. Morgenstern and Phukan (1969) fitted their data for Bunter sandstone samples (with porosities ranging from 10% to 17.5%) to the relation $\beta = c_1 - c_2 \log P$. Alternatively, an exponential decay relation was used by Zimmerman (1984), and he further interpreted such data by the progressive closure of a noninteractive ensemble of penny-shaped cracks (with aspect ratio α), such that the distribution function of porosity is given by $c(\alpha) = C\alpha \exp(-\alpha/\alpha^*)$, with $C = 5.29 \times 10^5$ and $\alpha^* = 7.54 \times 10^{-5}$ for the Berea sandstone and $C = 1.47 \times 10^5$ and $\alpha^* = 1.15 \times 10^{-4}$ for the Boise sandstone (Zimmerman, 1991). The inferred aspect ratios for these sandstones are on the order of 1×10^{-4}, with peaks located at α^*. On integrating the distributions, microcrack porosities of 0.30% and 0.19% are inferred for the Berea and Boise sandstones, which represent small fractions of the total porosites (equal to 22% and 25%, respectively).

In Figure 2.2 compressibility data for limestone and chalk with porosities ranging from 3% to 45% determined at an effective pressure of 30 MPa are compiled from published data (Vajdova et al., in press). As noted earlier, limestones seem to be stiffer than sandstones of comparable porosities. There is a somewhat clearer trend for compressibility to increase with increasing porosity. While microcrack closure has significant effect on the compressibility in a relatively compact rock

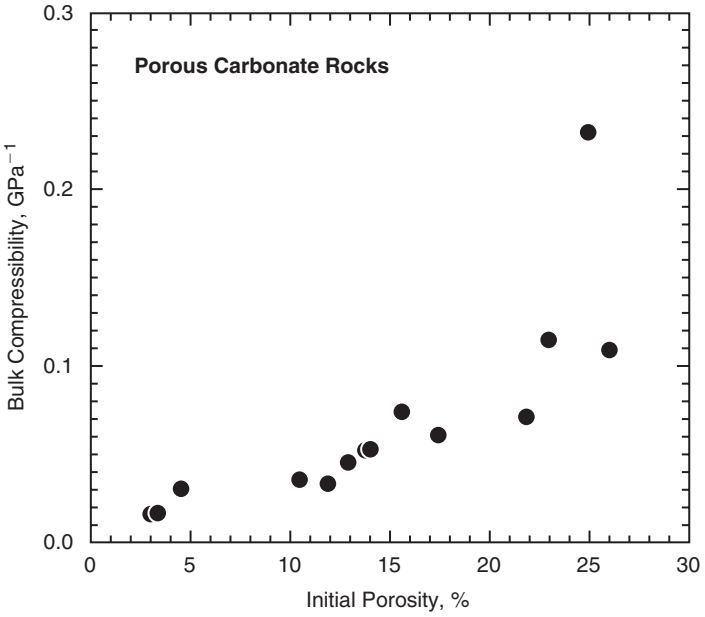

Figure 2.2 ► Compressibility of limestone and chalk as function of porosity at effective pressure of ≈30 MPa. The data compiled by Vajdova et al. (2003) indicate an overall increase of compressibility with porosity in carbonate rocks.

such as the Solnhofen limestone, the effect is minimal in more porous limestones beyond an effective pressure of 30 MPa or so.

To an extent, nonlinear elastic behavior can be described by a stress-dependent compressibility. However, such an approach has intrinsic limitation in the presence of appreciable inelastic deformation, commonly associated with pore collapse and grain crushing in porous rocks. In Figure 2.3 the bulk compressibility data for Boise sandstone and Indiana limestone are plotted as a function of effective pressure. In the Boise sandstone the inception of pore collapse and grain crushing at an effective pressure of ≈75 MPa induced the compressibility to apparently increase by one order of magnitude. Furthermore, significant irreversible strain, acoustic emission (AE) activity, and permeability reduction are observed when the sample is stressed to beyond this critical pressure (Zhang et al., 1990b; David et al., 1994). Analogous behavior has been observed in carbonate rocks (Vajdova et al., in press). During uniaxial-strain tests qualitatively similar behavior was also

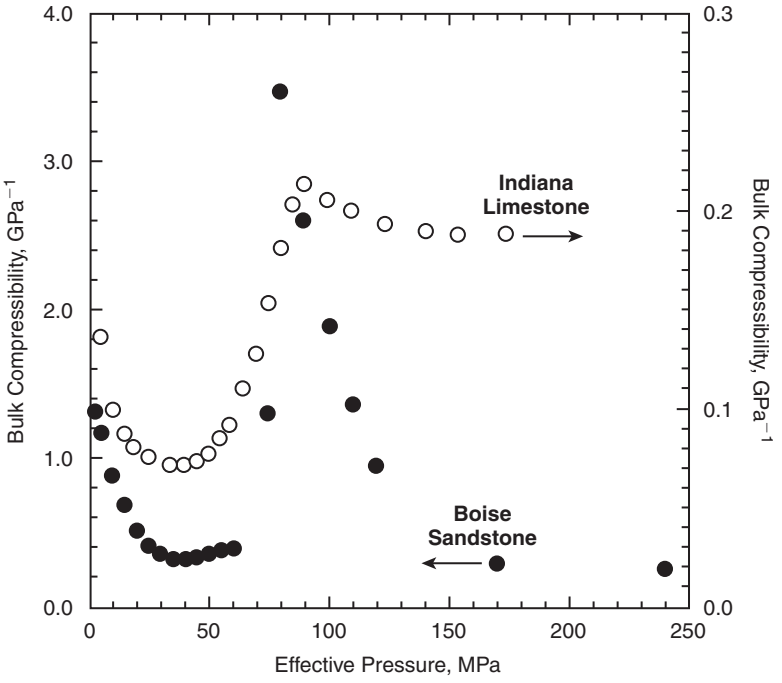

Figure 2.3 ► Compressibilities of Boise sandstone (Zhang et al., 1990b) and Indiana limestone (Vajdova et al., in press) as functions of effective pressure. The closure of microcracks results in an initial decrease of compressibility with pressurization, which is followed by a dramatic increase due to the onset of pore collapse. The compressibility decreases again with the progressive development of pore collapse.

reported by Smits et al. (1988) in chalk and by Schutjens and de Ruig (1997) in sandstones.

2.2.2 Inelastic Behavior and Failure Mode

If the deformation involves significant irreversible strain and if the failure mode is localized, then it is unlikely that a poroelastic model can capture the fundamental attributes of the mechanics. Plasticity theory provides a useful constitutive framework for describing the macroscopic behavior in such an inelastic continuum (Chapter 1). A phenomenological model should account for several key features of the inelastic compaction behavior of a rock.

- Inelastic deformation may be appreciable even in the absence of any deviatoric stresses. Significant damage may accumulate in response to purely hydrostatic loading (due to an increase in confining pressure or decrease in pore pressure).
- A deviatoric stress field promotes the onset and development of inelastic compaction. If we compare the porosity reductions in two systems subjected to identical effective mean stress, compaction in a nonhydrostatically loaded system is enhanced relative to that in a hydrostatically loaded system. This phenomenon is referred to as shear-enhanced compaction.
- While shear localization is often inhibited by compaction (and promoted by dilatancy), recent studies have shown that several modes of localized failure can be pervasive in a compactant rock.

Hydrostatic Compaction

Figure 2.4 illustrates the hydrostatic compaction behavior for seven sandstones with porosities ranging from 14% to 35% (Zhang et al., 1990a; David et al., 1994; Wong et al., 1997). Typically, the mechanical response of a porous sandstone is nonlinear even for the elastic regime. Under hydrostatic loading, the pore space is initially tightened by elastic deformation, and as a result, it becomes more and more stiff, as manifested by a decrease in the compressibility (Figure 2.3). However, as the hydrostatic loading increases, the sample reaches a point where it suddenly becomes more compliant, showing a dramatic increase in compaction. If a sample is loaded beyond this inflection point and then unloaded, the permanent compaction is significant. This inflection point P^* occurs at a wide range of pressures, from 80 MPa to 400 MPa for the seven sandstones in Figure 2.4.

In a siliciclastic rock the inflection point in the hydrostatic compaction curve is manifested in the microstructure by the onset of grain crushing (Zhang et al., 1990a; Menéndez et al., 1996). The local stresses at impinging grain contacts are sufficiently high that extensile microcracks nucleate and propagate across the grains, manifested by marked enhancement of AE activity (Zhang et al., 1990b; David et al., 1994). The grains are crushed and the pores collapse, resulting in

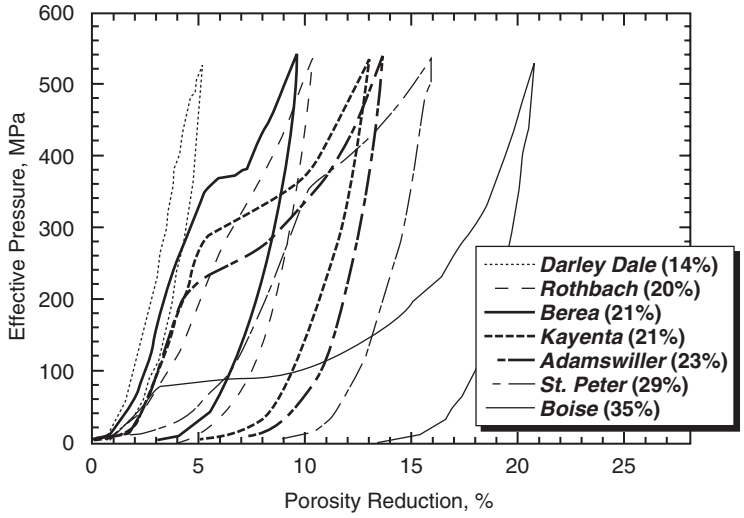

Figure 2.4 ► Hydrostatic compression of seven sandstones. Each of the hydrostats shows a sharp inflection point, which corresponds to the critical effective pressure P^* for the onset of grain crushing and pore collapse. The experiments were conducted on samples saturated with distilled water and under drained conditions. The nominal porosity of each sandstone follows its name.

an overall decrease in porosity. Noting that the magnitude of P^* is primarily controlled by the porosity ϕ and grain size R, Zhang et al. (1990a) formulated a Hertzian fracture model, in which the porous rock is idealized as a randomly packed assemblage of spherical particles of several distinct sizes. This micromechanical model for grain crushing predicts that $P^* \prec (\phi R)^n$, with $n = -1.5$. In a later section, we will elaborate on the mathematical formulation of this model. Wong et al. (1997) presented a compilation of the grain crushing pressure P^* as a function of initial porosity ϕ and grain radius R, and it can be seen in Figure 2.5 that the sandstone data are in basic agreement with the Hertzian fracture model. A similar trend has also been observed in unconsolidated materials (including sand and glass spheres) (Wong et al., 1997).

The inelastic compression behavior in a carbonate rock is qualitatively similar, as illustrated by the hydrostat for the Indiana limestone (Figure 2.6). The compilation of Vajdova et al. (in press) shows that there is an overall trend for the critical pressure to decrease with increasing porosity: P^* significantly decreases in the porosity range of 3% to 15%, followed by a more gradual decrease in the range of 15% to 45% (Figure 2.7a). Since pore collapse in a carbonate rock seems not to involve appreciable grain-scale cracking as conceptualized in the Hertzian fracture model, Baud et al. (2000b) proposed as an alternative the use of a model that appeals to plastic collapse of spherical pores (Curran and Carroll, 1979). For a rock in which crystal plasticity processes (such as mechanical twinning and dislocation

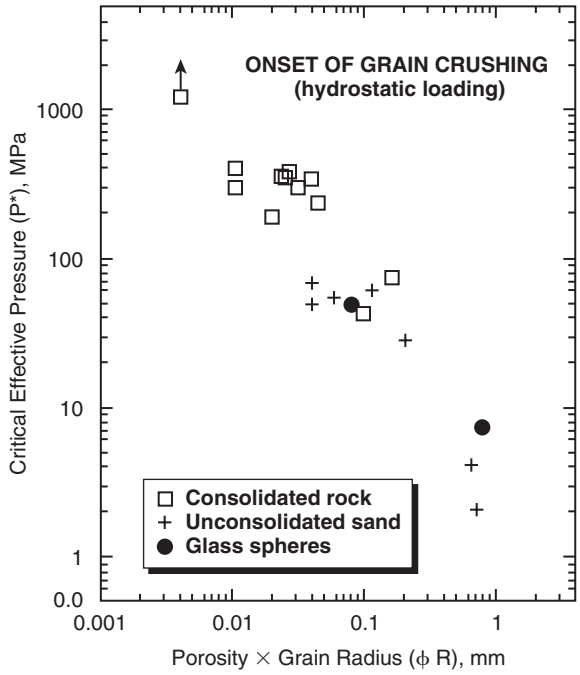

Figure 2.5 ► Critical effective pressure (P^*) for the onset of grain crushing in sandstone as a function of initial porosity and grain radius. The data follow an approximately linear trend with a slope of $-3/2$, in accordance with equation 2.9.

slip in calcite) are dominant, the applied stress field induces stress concentration in the vicinity of the spherical pore, and plastic flow occurs if the local stress field satisfies a specified yield condition.

For hydrostatic loading this plastic-collapse model predicts that initial yield (corresponding to the onset of plastic collapse) occurs at the macroscopic critical pressure $P^* = (2/3)Y\{1 - 2\mu\phi/[2\mu + Y(1-\phi)]\}$, where Y is the plastic yield stress for uniaxial loading. If the critical pressure and porosity data from Figure 2.7a are substituted into this equation, this model predicts that the yield stress would decrease with increasing porosity as shown in Figure 2.7b.

Shear-Enhanced Compaction and the Transition from Brittle Faulting to Ductile Flow

When subjected to an overall compressive loading, a porous rock may fail by shear localization or by cataclastic flow. The mechanical response to isotropic (or hydrostatic) loading and to anisotropic loading is fundamentally different. While hydrostatic loading always gives rise to compaction, whether porosity decreases or

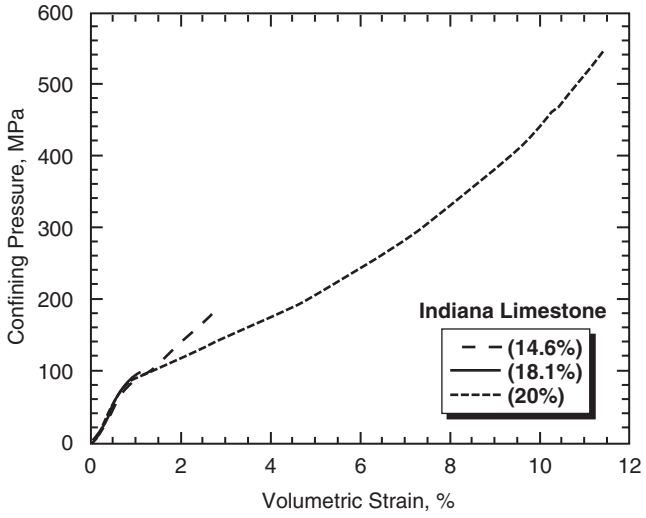

Figure 2.6 ► Hydrostatic compression of three nominally dry samples of Indiana sandstones, with initial porosities of 14.6%, 18.1%, and 20.0%. Each hydrostat shows an inflection point that corresponds to the critical effective pressure P^* for the onset of pore collapse.

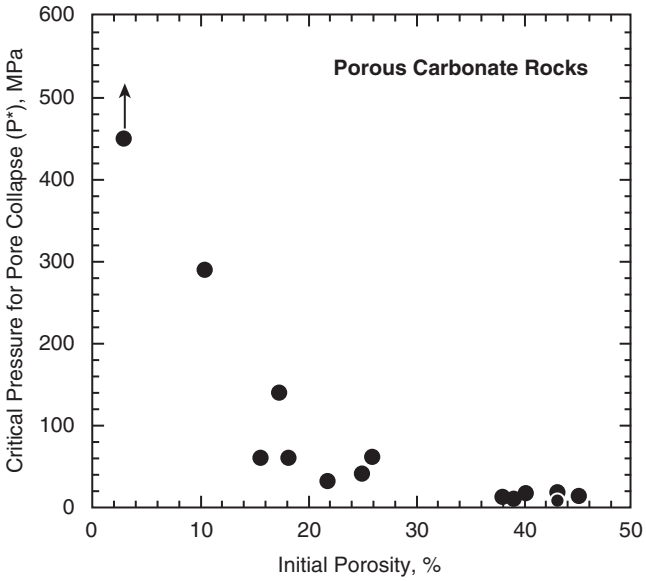

Figure 2.7a ► (a) Critical effective pressure (P^*) for the onset of pore collapse in carbonate rocks as a function of initial porosity. The data compiled by Vajdova et al. indicate an overall decrease of the pore collapse pressure with increasing porosity.

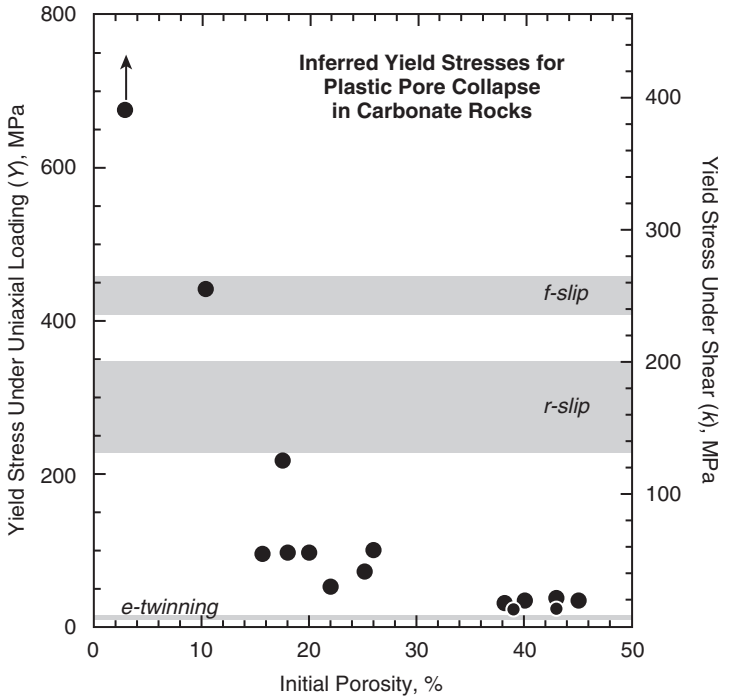

Figure 2.7b ► (b) If the P^* data correspond to the onset of crystal plasticity processes in the solid grains, then Curran and Carroll's (1979) plastic collapse model can be used to infer the yield stress Y as a function of porosity. For reference, the yield stresses that have been determined for specific mechanisms are also shown. This comparison suggests that pore collapse in highly porous carbonate rocks (with porosities >15% or so) predominately involves mechanical twinning, whereas dislocation slip processes dominate in the more compact and fine-grained limestones.

increases in response to a deviatoric stress field depends on the trade-off between pore collapse mechanisms and the counteracting tendency for microcracking to dilate the sample. Compaction may persist over large strain only if the multiplicity of microcracks do not coalesce to result in shear localization.

Wong and Baud (1999) have presented a comprehensive review of inelastic compaction in porous sandstones. The compaction and failure mode are illustrated in Figure 2.8 by the mechanical data for Adamswiller sandstone of initial porosity 23% (from Wong et al. (1997)). The top graph shows the differential stress $\sigma_1 - \sigma_3$ versus the axial strain for six triaxial compression experiments at a fixed pore pressure of 10 MPa and confining pressures fixed at six values as indicated. The bottom graph shows porosity decrease versus axial strain for the same samples. The samples deformed at effective pressures of 5 MPa and

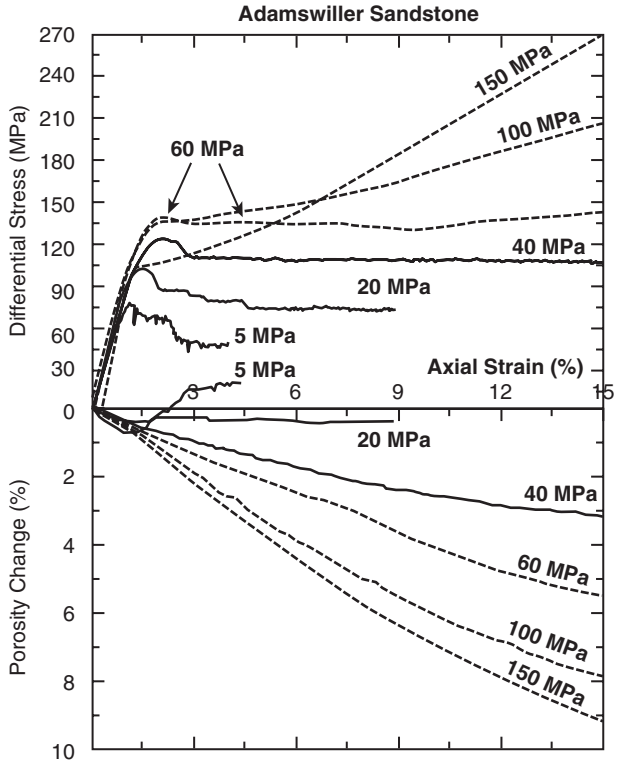

Figure 2.8 ► Mechanical data for saturated Adamswiller sandstone. Differential stress and porosity change are plotted versus axial strain, and the effective confining pressures are as indicated. The solid curves are for samples that failed by shear localization; dashed curves are for samples that failed by cataclastic flow, with delocalized compaction and strain hardening.

20 MPa are representative of the brittle faulting regime. The differential stress attained a peak, beyond which strain softening was observed and the stress progressively dropped to a residual level. The peak stress shows a positive correlation with effective pressure, which is typical of Mohr-Coulomb type of brittle failure. The porosity initially decreased, but near the peak stress it reversed to an increase indicating dilation of the pore space. The dilation decreased with increasing effective pressure. Visual inspection of post-peak samples confirmed that they failed by shear localization, with a throughgoing shear band cutting across each sample.

The dashed curves (for samples deformed at effective pressures of 60, 100, and 150 MPa) are representative of the compactive cataclastic flow regime. The slopes of the differential stress–axial strain curve were nonnegative, and the

porosity decreased monotonically with deformation. Shear localization was not evident in samples deformed to an axial strain of up to 30%. The sample deformed at 40 MPa showed a peak stress and strain softening, but the porosity persistently decreased with deformation. This "transitional" mode of failure is manifested by various complex localization phenomena that will be discussed in a later section.

Additional insights are gained by plotting the effective mean stress $(\sigma_1 + 2\sigma_3)/3 - p$ versus the porosity change (Figure 2.9). For reference, the hydrostat is also shown (as the dashed curves). In a conventional triaxial compression experiment, the nonhydrostatic and hydrostatic loadings are coupled. If the axial stress increases by an increment $\Delta\sigma_1$ while the confining and pore pressures are maintained constant, then the effective mean stress and differential stress would increase by the amounts $\Delta\sigma_1/3$ and $\Delta\sigma_1$, respectively. If the porosity change is solely controlled by the hydrostatic stresses, then the triaxial data (solid curves) should coincide with the hydrostat (dashed curves). Deviations from the hydrostat would imply that the porosity change depends on not only the effective mean stress, but also the deviatoric stresses. In the cataclastic flow regime, the triaxial curve for a given effective pressure coincided with the hydrostat up to a critical stress state (indicated by C^* in Figure 2.9b), beyond which there was an accelerated decrease in porosity in comparison the hydrostat. At stress levels beyond C^* the deviatoric stress field provided significant contribution to the compactive strain, and this phenomenon is referred to as shear-enhanced compaction (Curran and Carroll, 1979; Wong et al., 1992). In contrast, the porosity-change behavior at effective pressures of 5 and 20 MPa was such that the compaction decelerated in comparison with the hydrostat beyond critical stress states marked as C' (Figure 2.9a). This implies that at stress levels beyond C' the deviatoric stress field induced dilatancy.

The critical stress levels for the onset of shear-enhanced compaction varies significantly among sandstones. Data for six sandstones with porosities ranging from 15% to 35% (from Wong et al., [1997]) are shown in Figure 2.10 in the stress space, with coordinates given by the effective mean stress $P = (\sigma_1 + 2\sigma_3)/3 - p$ and the differential stress $Q = \sigma_1 - \sigma_3$. For reference, the peak stresses (for brittle fracture under relatively low effective pressures) are also included as open symbols. The C^* data (solid symbols) map out the compactive yield envelopes for the onset of shear-enhanced compaction, which is manifested by a negative correlation between P and Q at the critical stress states. The brittle–ductile transition is associated with the stress state at the intersection of this compactive yield envelope with the Mohr-Coulomb envelope for brittle faulting.

The data compiled for various sandstones underscore that shear-enhanced compaction and cataclastic flow can occur over a broad range of stress conditions. The compactive yield envelope of Berea sandstone has stress values more than five times greater than those of Boise sandstone. Since the former has a porosity of 21% and the latter a porosity of 35%, one may infer that porosity exerts important influence over the compactive yield behavior. However, other microstructural

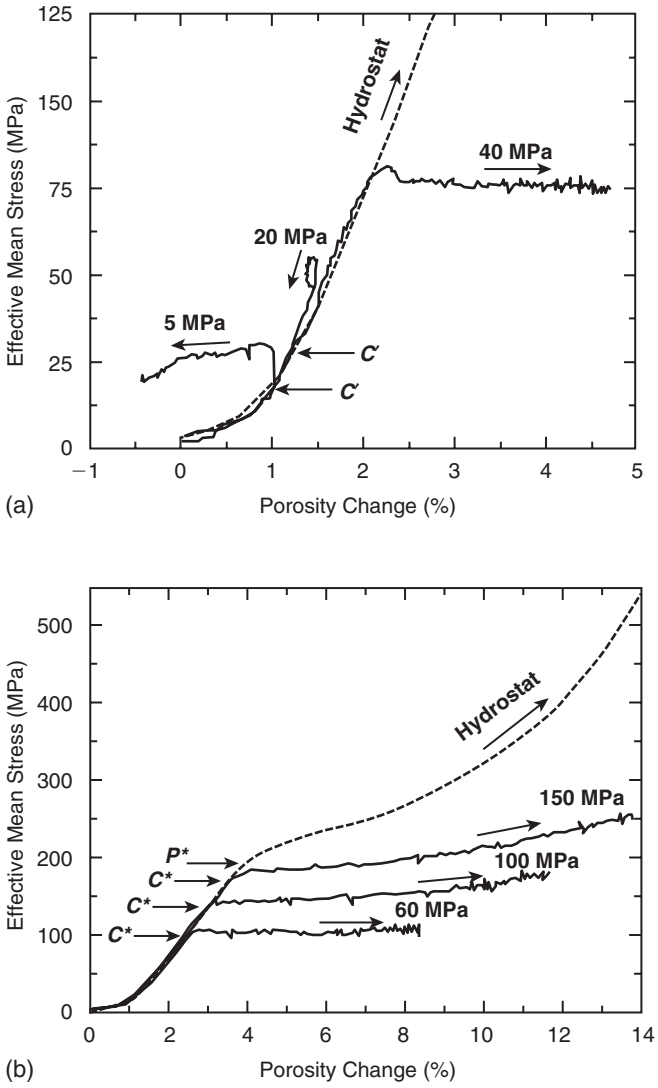

Figure 2.9a-b ► (a) Shear-induced dilation and (b) compaction in saturated Adamswiller sandstone. The solid curves show the effective mean stress as a function of porosity change for triaxial compression tests at fixed effective pressures, as indicated. For reference, the hydrostat is shown as dashed curves. The critical stress states C' and C^* are indicated by open arrows.

parameters (such as grain size, cementation, and clay content) may also be important since there is considerable discrepancy between the yield envelopes of Berea and Kayenta sandstones, both of which have porosity of 21%.

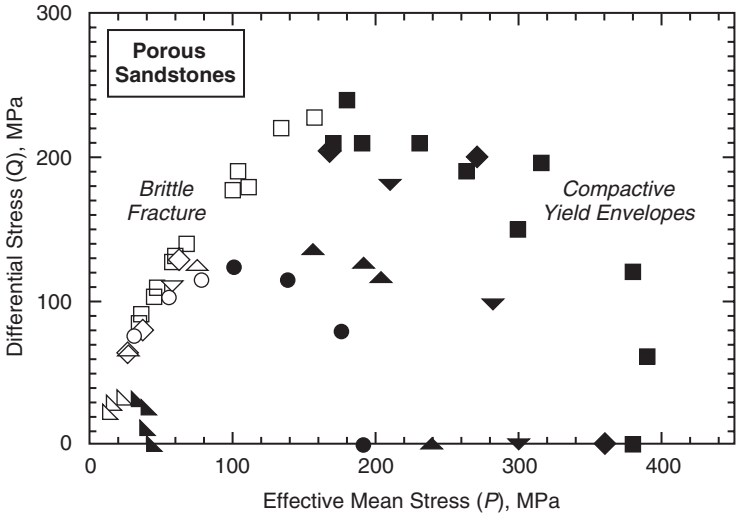

Figure 2.10 ► Stress state C^* at the onset of shear-enhanced compaction (solid symbols) and peak stress for brittle fracture (open symbols) are shown in the P (effective mean stress) and Q (differential stress) space. Note that the compactive yield envelopes have approximately elliptical shapes. Data for six saturated sandstones are shown.

Since one end of the compactive yield envelope is "anchored" at a location on the P-axis corresponding to P^*, this implies that if a siliciclastic rock requires a relatively high effective pressure for grain crushing to occur, then the critical stress states C^* for the onset of shear-enhanced compaction are also expected to be high. In other words, the grain crushing pressure P^* acts as a scaling parameter for the magnitudes of the compactive yield stresses C^*, and in this sense the critical pressure P^* provides a quantitative measure of the "brittleness" of a porous siliciclastic rock (Wong et al., 1997). Compactive yield envelopes of similar shape have been widely observed in soil (Chen, 1984; Desai and Siriwardane, 1984), and plasticity formulations such as the critical state (Schofield and Wroth, 1968) and cap (DiMaggio and Sandler, 1971) models have provided a constitutive framework for analyzing the inelastic deformation and failure. Such plasticity formulations are discussed in Chapter 1. Wong et al. (1997) showed that the sandstone data can be described by an elliptical cap in the P–Q stress space:

$$\frac{(P/P^* - \xi)^2}{(1-\xi)^2} + \frac{(Q/P^*)^2}{\zeta^2} = 1 \tag{2.2}$$

with $\xi \approx 0.5$ and ζ between 0.5 and 0.7. Since microstructural parameters (such as porosity ϕ and grain size R) exert control over the hydrostatic grain crushing process in accordance with the power law $P^* \prec (\phi R)^n$, they should similarly influence the compactive yield envelope since the stress invariants in 2.2 are normalized

with respect to P^*. This implies that the yield envelope for onset of shear-enhanced compaction in a sandstone expands with decreasing porosity and grain size.

If the normality condition is assumed, then from the yield condition of equation 2.2 we can follow the formalism described in Chapter 1 to derive the plastic strain increments once yielding has begun. For axisymmetric loading Wong et al. (1997) introduced an inelastic compaction factor $CF = \Delta\Phi^p/\Delta\varepsilon^p$ that corresponds to the ratio between incremental changes of plastic components of the porosity and axial strain, which for the elliptical cap is given by

$$CF = \frac{\Delta\Phi^p}{\Delta\varepsilon^p} = 3 - \frac{3}{1 + [\zeta/(1-\xi)]^2\,[(P - \xi P^*)/(3Q)]} \tag{2.3}$$

For hydrostatic loading the compaction factor attains its maximum value of 3 when the effective pressure equals the critical crushing pressure P^*. At a lower effective pressure, a differential stress ($Q > 0$) is necessary for the onset of shear-enhanced compaction, and the normality condition requires a compaction factor that is significantly lower than 3. The laboratory data for sandstone samples that failed by delocalized cataclastic flow are comparable in magnitude to the theoretical prediction (Wong et al., 1997). Studies on carbonate rocks (Elliot and Brown, 1985) and saline ice (Schulson and Nickolayev, 1995) indicate similar agreement between experiment and theory. However, at lower effective pressures ($\approx 0.5\ P^*$) near the brittle–ductile transition, experimental measurements of inelastic compaction in the transitional regime show appreciable discrepancy with predictions of an associative flow rule that assumes normality (Wong et al., 2001).

The phenomenology of shear-enhanced compaction and brittle–ductile transition in porous carbonate rocks is similar to that in siliciclastic rocks. Nevertheless, the carbonate rocks also have several distinct attributes that should be noted.

- Shear-enhanced compaction can occur in a carbonate rock at very low porosities. Baud et al. (2000b) documented the compaction behavior in the Solnhofen limestone with initial porosity of 3%. This implies that pore collapse is a fairly common deformation process that can occur even in carbonate rocks considered to be relatively compact.
- The compactive yield behavior in carbonate rocks seems to be primarily controlled by the porosity, as illustrated by the compactive yield stress data compiled by Vajdova et al. (in press) for limestone and chalk with porosities ranging from 3% to 54%. We show in Figure 2.11 the caps for Indiana limestone (Vajdova et al., in press), Bath stone (Elliot and Brown, 1985), and Lixhe chalk (Homand and Shao, 2000). A micromechanical model for plastic pore collapse described in a later section can be used to describe such data.
- In limestones it is commonly observed that compaction is a transient precursor to the inception of dilatancy. As illustrated in Figure 2.12a the Solnhofen sample switched from compaction to dilation (at the stress state marked as $C^{*\prime}$) after it had undergone a certain amount of strain hardening. Mapped in

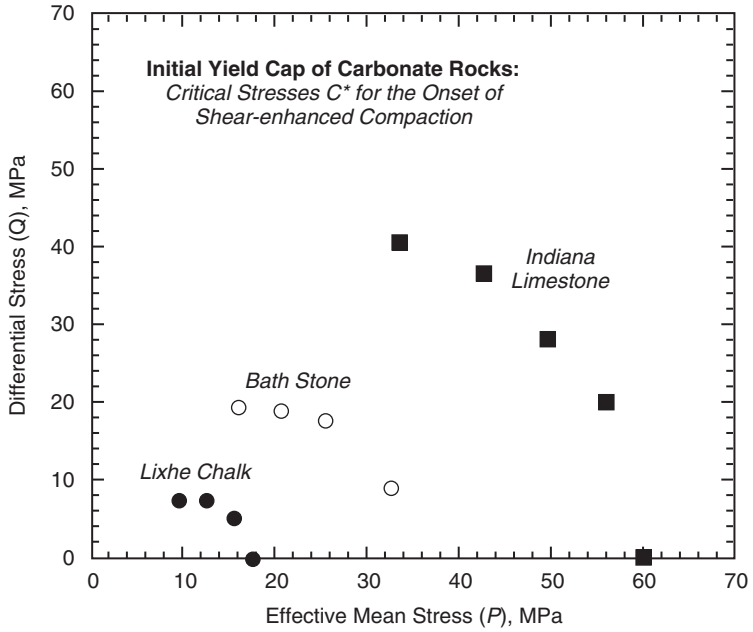

Figure 2.11 ► Stress state C^* at the onset of shear-enhanced compaction are shown in the P (effective mean stress) and Q (differential stress) space. Data for three carbonate rocks with porosities of 15.6% (Indiana limestone), 22.9% (Bath stone), and 43% (Lixhe chalk) are shown.

the stress space (Figure 2.12b), the yield stresses for shear-enhanced compaction in the limestone are initially described by a cap with negative slope that expands with strain hardening, gradually evolving to a dilatant yield envelope with positive slope. Similar behavior has been observed in the Tavel and Indiana limestones with porosities of 11% and 18%, respectively (Vajdova et al., in press).

The rock deformation data summarized here provide important constraints on the formulation of constitutive models for many geological and geotechnical problems. The mathematical formalism by which these yield relations and mechanical data can be applied in a continuum plasticity model and localization analysis is presented in Chapter 1 and Chapter 5, respectively.

Influence of Fluid on Mechanical Compaction

Aqueous pore fluid exerts significant mechanical and chemical effects on virtually all crustal processes. Previous studies have shown that brittle strength of a rock is generally reduced in the presence of water. The water-weakening effect may arise

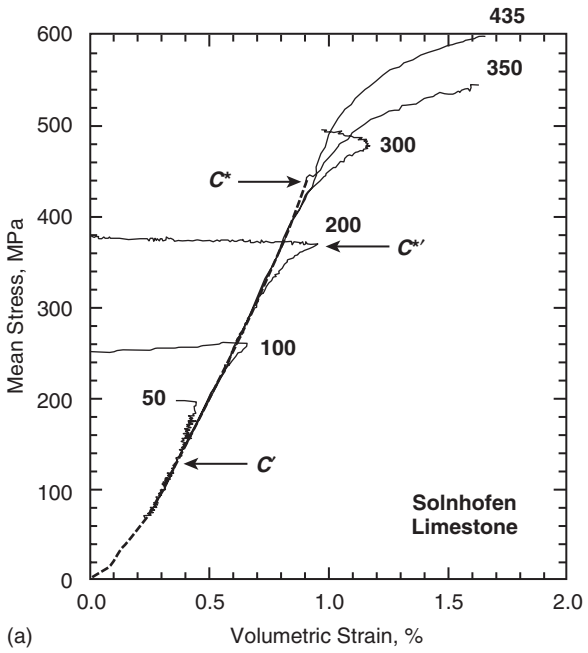

Figure 2.12a ► (a) Mechanical data from triaxial compression experiments of Baud et al. (2000b) on Solnhofen limestone. Volumetric strain is plotted versus mean stress, and the confining pressure (in MPa) is indicated on each curve. For reference, the hydrostat is shown as heavy dashed line. The critical stress states for dilatancy C', onset of shear-enhanced compaction C^*, and transition from shear-enhanced compaction to dilatancy $C^{*\prime}$ are indicated by the arrows for experiments performed at confining pressures of 50, 300, and 200 MPa, respectively.

from two mechanisms. First, the mechanical role of pressurized pore fluid tends to weaken and embrittle rocks (Paterson, 1978; Guéguen and Palciauskas, 1994). The mechanical effect of fluid pressure is elaborated in Chapters 1 and 4. Second, the chemical influence of pore fluids is to further weaken the rock through a reduction of surface free energy (Rehbinder et al., 1948; Orowan, 1944), a subcritical cracking mechanism such as stress corrosion (Atkinson and Meredith, 1987), or both combined. Capillary forces may also contribute significantly to the rock compaction when different fluids are present in the rock pore space (Schroeder et al., 1998). Diffusive mass transfer may also be involved, but since pressure solution is discussed in Chapter 3, we will not consider this chemical compaction mechanism here.

While previous experimental studies on the chemical effect have focused on reduction of the brittle strength in the presence of water (Lajtai et al., 1987; Chester and Logan, 1986; Hadizadeh and Law, 1991), Baud et al. (2000b) investigated

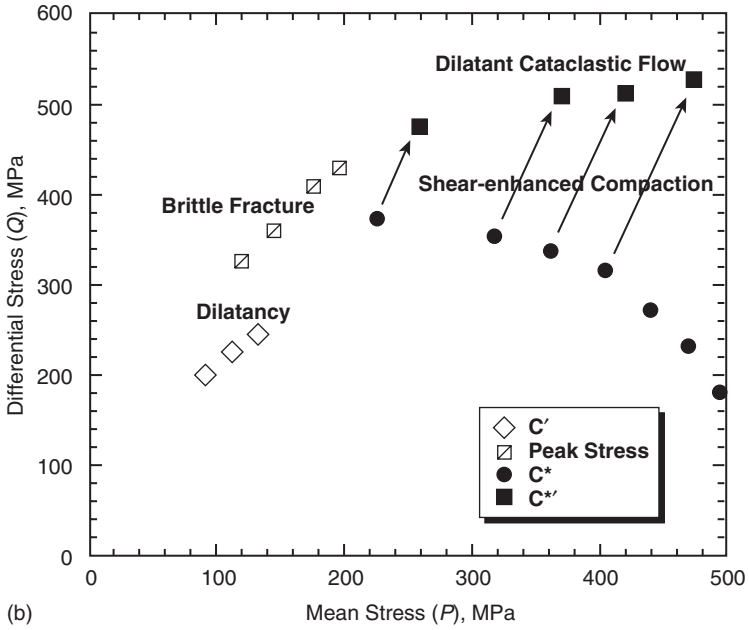

Figure 2.12b ► (b) The stress states C', C^*, and $C^{*\prime}$ and brittle strength are shown in the P-Q space for the Solnhofen limestone data. Three regimes of inelastic and failure modes can be identified: brittle fracture, dilatant cataclastic flow, and shear-enhanced compaction.

water-weakening effect on compactive failure in the Berea, Boise, Darley Dale, and Gosford sandstones (with nominal porosities ranging from 11% to 35%). Figure 2.13 contrasts the data for Darley Dale sandstone samples (under nominally dry and saturated conditions) at effective pressures ranging from 10 MPa to 300 MPa. The inelastic behavior and failure mode of nominally dry samples were qualitatively similar to those of water-saturated samples. At elevated pressures shear localization was inhibited and all the samples failed by strain hardening. The compactive yield strengths (associated with the onset of shear-enhanced compaction) of the nominally dry and saturated samples are compiled in Figure 2.14. The yield stresses at the onset of shear-enhanced compaction for the nominally dry samples can also be described by elliptical envelopes (equation 2.2). It can be seen that the envelopes for the wet samples are lower than those in the dry samples deformed under comparable pressure conditions by 20% to 70%. In comparison the water-weakening of brittle strength in these sandstones ranged from 5% to 17%. The water-weakening effects (for both brittle faulting and compactive failure regimes) were most and least significant in the Gosford and Berea sandstones, respectively. Baud et al. (2000a) demonstrated that water-weakening effects in both regimes can be explained consistently by micromechanical models formulated on

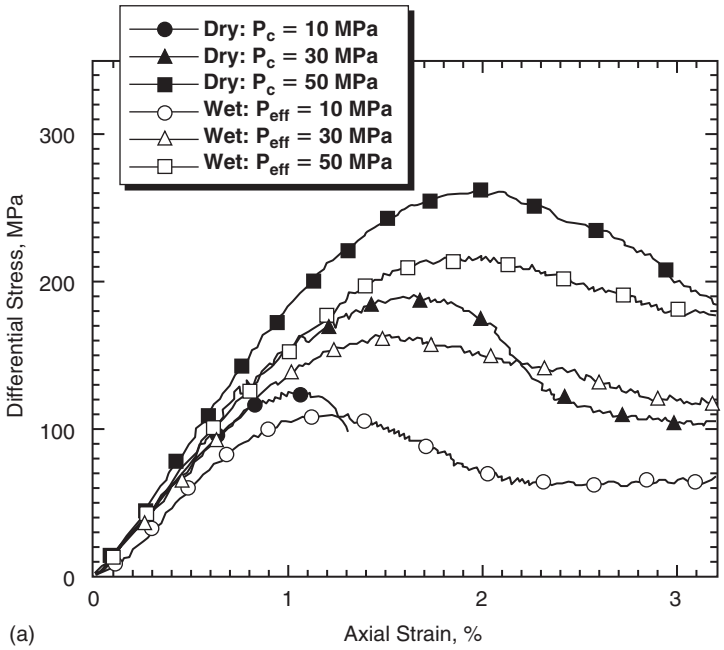

Figure 2.13a ► (a) Mechanical data of Darley Dale sandstone for samples deformed in the (a) brittle regime and

the basis that the specific surface energy in the presence of water is lower than that in vacuo. The micromechanics will be addressed in a later section.

There are many geophysical and geotechnical applications in which the pore space may be partially saturated. In such cases, the mechanical behavior may be influenced by capillary actions (Lawn, 1993). Schmitt et al. (1994) reported appreciable strengthening in partially saturated samples of Fontainebleau sandstone during uniaxial compression tests. In contrast, Baud et al. (2000a) reported that while a moderate strengthening effect was observed during triaxial compression in a Darley Dale sandstone sample with 15% saturation, the effect was negligible in samples with higher degrees of saturation.

For carbonate rocks the influence of fluid has not been studied in such a detailed manner. Nevertheless, data for limestone and chalk over a range of porosities indicate that the weakening effect can be appreciable in both the compactive failure and brittle faulting regimes. Rutter (1974) contrasted the compactive failure behavior in saturated and dry samples of Solnhofen limestone (with initial porosity of 5.8%), and he concluded that the strength and work hardening rate were lowered appreciably in the presence of water. Boozer et al. (1963) reported that the compactive failure and brittle faulting behavior of Indiana limestone (with initial porosity of 16%) was affected by two fluids (oleic acid and saturated calcium

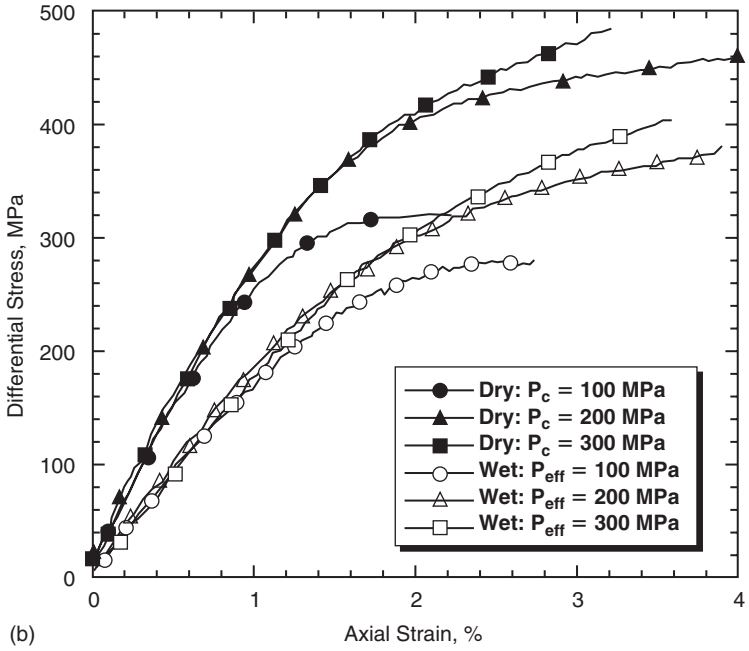

Figure 2.13b ► (b) cataclastic flow regime. Differential stress is plotted versus axial strain. The open symbols are for water-saturated samples and the closed symbols are for the nominally dry samples.

carbonate solution), which are strongly adsorbed on the grain surface. The strengths in these samples were significantly lower than those of samples saturated with the chemically inert *n*-hexadecane and dry samples. Similar behavior has also been observed in chalk. The strengths of oil-saturated samples of the Lixhe chalk (with a porosity of ∽40%) are reported to be almost twice those of water-saturated samples (Risnes et al., 1996; Homand and Shao, 2000).

Influence of Cement

We have so far focused on the influences of two microstructural parameters, namely porosity and grain size. However, other microstructural parameters, including cementation and clay content, may also exert important influences on mechanical compaction. The importance of cementation has long been recognized. Dvorkin and coworkers (Dvorkin et al., 1991, 1994; Yin and Dvorkin, 1994) have conducted comprehensive analyses of the significant effects of cementation on elastic and inelastic behavior of sedimentary rocks. In an experimental study the effect of cementation on dilatant and compactive failure was systematically quantified on synthetic sandstones made from a mixture of silica sand grains (Fontainebleau

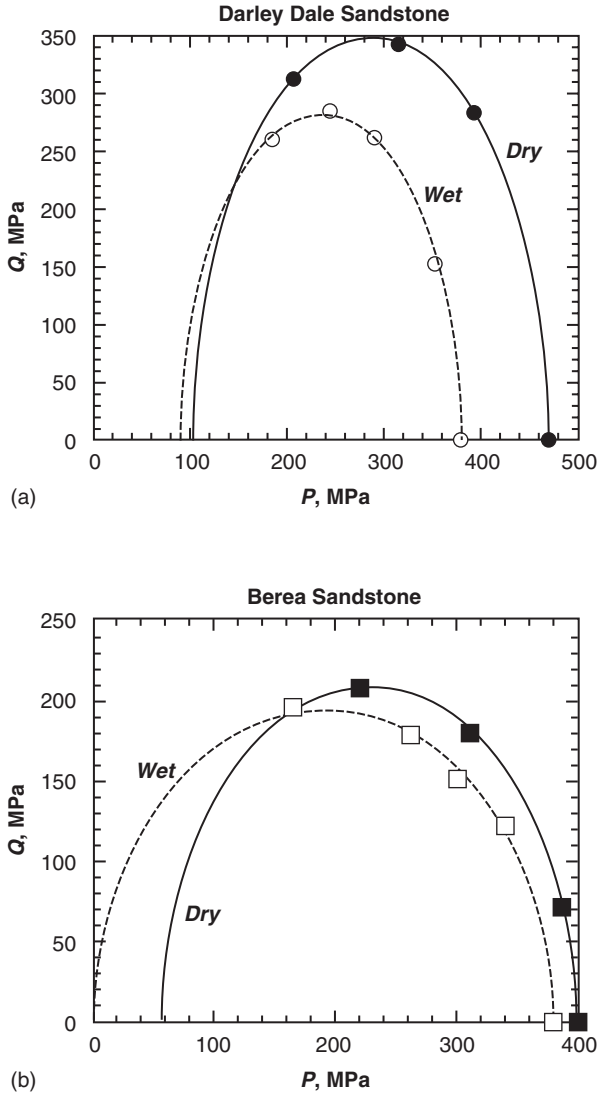

Figure 2.14a-b ►

sand) and silica gel, using a hot-pressing technique (den Brok et al., 1997). By changing the amount of silica gel in the mixture before hot-pressing and while holding constant other petrophysical parameters such as grain size, sorting, and mineralogical content, it was possible to isolate the effect of cementation on the mechanical and physical properties of the synthetic sandstones. Two batches of sandstone-like material were prepared, corresponding to a volumetric cement content of 3% and 5%, respectively. The synthetic sandstones were then tested under

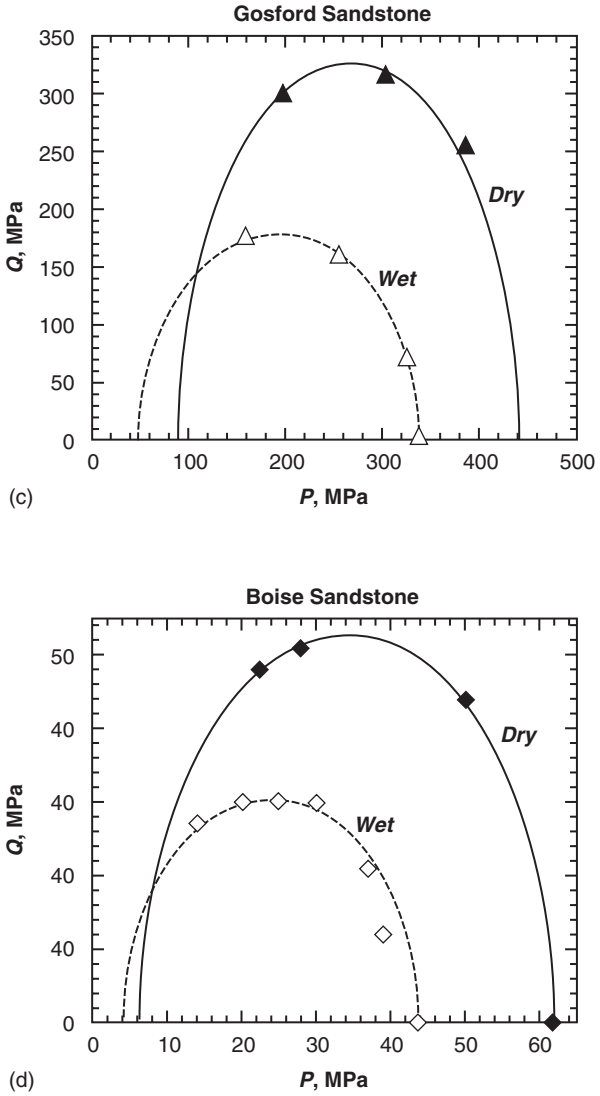

Figure 2.14a-b-c-d ► Compactive yield stresses at the onset of shear-enhanced compaction for four sandstones in dry and wet conditions. Elliptical envelopes were used to fit the initial yield envelopes.

both hydrostatic and triaxial compression (David et al., 1998). The main results were the following:

► The experiments conducted under hydrostatic loading show that increasing the amount of cement from 3% to 5% in volume results in an increase of

the critical pressure P^*, to 380 MPa for material of 3% volumetric cement content; to >450 MPa for 5%.

- The experiments conducted under triaxial conditions show that increasing the cement content raises mechanical resistance as well as the elastic moduli by 20% on average. To illustrate this point, we present in Figure 2.15 the mechanical data for two samples tested under the same experimental conditions.
- The brittle-to-ductile transition is shifted toward higher pressures when cementation is higher. For example, if we consider the experiments shown in Figure 2.15, the more cemented sample has typically a brittle behavior (dilatancy, significant stress drop, macroscopic fracture). The less cemented sample tested under the same experimental conditions was monotonically compacting and did not show any significant stress drop, a behavior typical of the cataclastic ductile-flow regime as discussed previously.

The data on the synthetic sandstone corroborate microstructural observations of naturally occuring rocks that have been deformed. For Berea sandstone Menéndez et al. (1996) have observed that in samples that had undergone hydrostatic and shear-enhanced compaction, intragranular cracking, grain crushing, and pore collapse are intense in uncemented grains, whereas these micromechanical processes seem to be inhibited in the vicinity of cemented contacts. In their finite-element

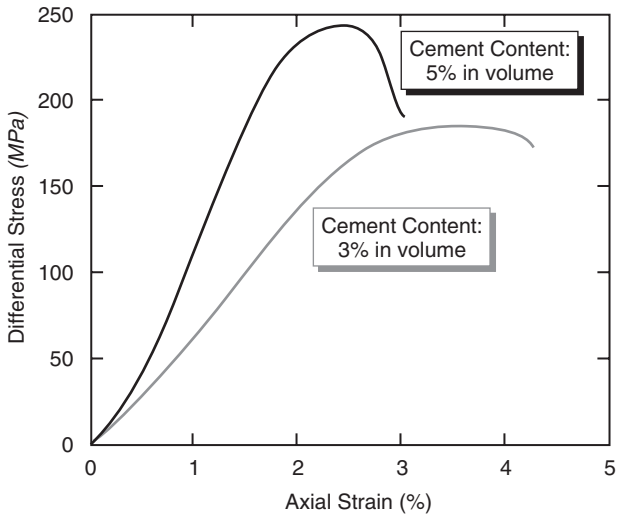

Figure 2.15 ► Comparison of the mechanical behavior of two synthetic sandstones with different cement content (David et al., 1998). In both cases, the triaxial experiments were conducted at 60 MPa confining pressure and 10 MPa pore pressure on water-saturated samples.

calculations, Wong and Wu (1995) have shown that the development of extensile cracking at cemented contacts would require an applied normal stress at least one order of magnitude greater than that for an uncemented contact. In addition, they showed that intergranular bonding, even with a very small amount of cement, is very efficient in reducing the tensile stress concentration at grain contacts. Hence they conclude that knowing the bulk volumetric fraction of cementing material is not enough to understand compaction because the distribution of microcracking and failure zones is strongly dependent on the location of cemented areas.

2.3 Micromechanics of Compaction

A realistic model of the micromechanics of compaction should be based on systematic microstructural observations, taking into account the heterogeneities on various scales. Rocks are characterized by a large variability of microstructural attributes (grain size and shape; pore size and shape; spatial distribution of grains, pores, and cracks, etc.) which all contribute to the heterogeneous nature of rocks. Consequently when deforming such heterogeneous media, the stress and strain fields can be analyzed by continuum mechanics only at a scale much larger than that of the microstructure. At small scale, all properties are highly variable, and averaging techniques or effective properties calculations can only be applied to regions larger than the so-called representative elementary volume (REV). For example, at the sample scale one can calculate average stresses and strains for a given loading scheme from measurements at external boundaries, but one has to keep in mind that any deformation or load applied on such boundaries is transferred and distributed within the rock through a complex framework of contacting bonds between grains or minerals.

In the past two decades, significant advances have been made in characterizing microstructural evolution during rock deformation. We first review the theoretical framework for analyzing the micromechanics of compaction, and then we summarize the microstructural observations that elucidate the damage mechanisms and provide constraints on the micromechanical models.

2.3.1 Theoretical Modeling of Grain Crushing and Pore Collapse

Heterogeneity of Contact Forces in Granular Materials

Relevant parameters to describe the properties of contacting bonds at the microstructure level are the contact geometry (flat, point load, rough surface, etc.), the elastic stiffnesses both normal and tangent to the contacting area, the elastic mismatch between contacting particles, and the nature and elastic properties of the cement if present. All these properties can present a large variability in

sedimentary rocks (Caruso et al., 1985; Pittman, 1984), giving rise to organized structures called "force chains" within the granular framework. To illustrate this point, we present here some results of numerical simulations using Particle Flow Code (two-dimensional version), a commercial software package now widely used in a number of applications by the geomechanics community (Cundall, 1971; Hazzard et al., 2000; Holt, 2001). In the two-dimensional model, a porous medium is represented by randomly packing several thousands of disks and specifying the disk and contact attributes and the overall porosity. We want to emphasize here the effect of contact stiffness distribution on the geometry and distribution of force chains within the granular framework. For that purpose the sample size and porosity (15%) are fixed, as well as the size distribution of particles, and assumed to be uniform. With these specifications, we compare in Figure 2.16 two situations:

- The homogeneous model (left), in which all the particles have the same normal stiffness $k_n = 5 \times 10^8$ N/m
- The heterogeneous model (right), in which a distribution of normal stiffnesses is considered: four classes of disks are involved, equally represented in the final assembly and corresponding to normal stiffness values of 5×10^7, 1×10^8, 5×10^8, and 1×10^9 N/m, respectively

The normal contact stiffness K_n between two particles A and B is then calculated by the relation $1/K_n = 1/k_n^{[A]} + 1/k_n^{[B]}$. Although the same seed is used for the random packing generation, the final assemblies differ slightly because the building process takes into account the local stiffnesses. The contact-bond model has been used, in which adjacent particles are bonded at their contact: consequently, a bond supports extensional forces up to a maximum value corresponding to the bond strength. After applying isotropic stress conditions on the "sample" boundaries, one can visualize the magnitude of contact forces within the assembly as shown in Figure 2.16 (the greater the thickness of the contact lines, the higher the normal contact force). It is clear that the contact forces are not homogeneously distributed, even when the local stiffness is constant: this is a consequence of the disorder introduced by the heterogeneity of the particle size distribution. In both realizations, there is a clear organization of the force chains: indeed, continuous thick lines delimitate individual cells that include several particles. Comparing both pictures, there are only subtle differences, but there seem to be more thick lines spreading over the investigated area in the heterogeneous case. Quantitatively, the statistics of contact forces in the case of isotropic loading are not significantly different: for both the homogeneous and heterogeneous assemblies, similar decreasing exponential-like histograms are obtained. This latter result is in agreement with previous studies on the statistics of contact forces in granular media (Makse et al., 2000).

The situation is different when an anisotropic stress field is applied to the sample: in that case many contacting bonds are subjected to extensional forces, and the statistical distribution of normal contact forces has a bell shape. For the heterogeneous model, the histogram is skewed toward larger compressive contact forces. Consequently, a higher elastic modulus and mechanical resistance are obtained for the heterogeneous granular assembly. It also exhibits more dilatancy than the homogeneous granular assembly. Pissarenko and Gland (2001) have shown that heterogeneity and geometrical disorder in granular media may result in a scale dependence of the mechanical properties, which has to be taken into account when scaling up from micromechanical studies. As more microscale heterogeneity is expected in natural granular rocks, some of the features observed on simple systems such as random packings of isotropic particles may be amplified, which makes it more difficult to study mechanical properties of granular rocks. One important feature worth emphasizing is that a limited number of particles support a significant part of the applied load: such a heterogeneous structure will obviously have strong consequences on local failure processes and strain localization.

Elastic Contact Theory

When increasing stresses are applied to a granular material, it is important to analyze the stress field at the microscale level to assess the mechanical stability conditions of the rock-forming minerals. As was mentioned before, this is a challenging task because of the heterogeneity commonly prevailing in rocks. The Hertzian contact theory gives the complete analytical solution for the stress distribution in the vicinity of the contact between isotropic elastic bodies. Originally, the theory was developed for torsionless loading over a frictionless planar area and was later extended to solids of revolution. We consider the case of two spheres with different properties, initially contacting at a single point (Figure 2.17a). A sphere with index i has a radius R_i and is made of a material with Young modulus E_i and Poisson ratio ν_i. When a force F is applied in the direction normal to the contact, the distance between the spheres is reduced and the contact area increases: for spherical particles, the contact region is a disk with radius a derived from the following relation (Mindlin, 1949):

$$a^3 = \frac{3FR_r}{4}\left[\frac{(1-\nu_1)^2}{E_1} + \frac{(1-\nu_2)^2}{E_2}\right], \tag{2.4}$$

where R_r is the relative radius of curvature given by $1/R_r = 1/R_1 + 1/R_2$. For two identical spherical bodies with radius R, made of the same material with elastic moduli E and ν, equation (2.4) becomes

$$a = \left[\frac{3\left(1-\nu^2\right)FR}{4E}\right]^{1/3}. \tag{2.5}$$

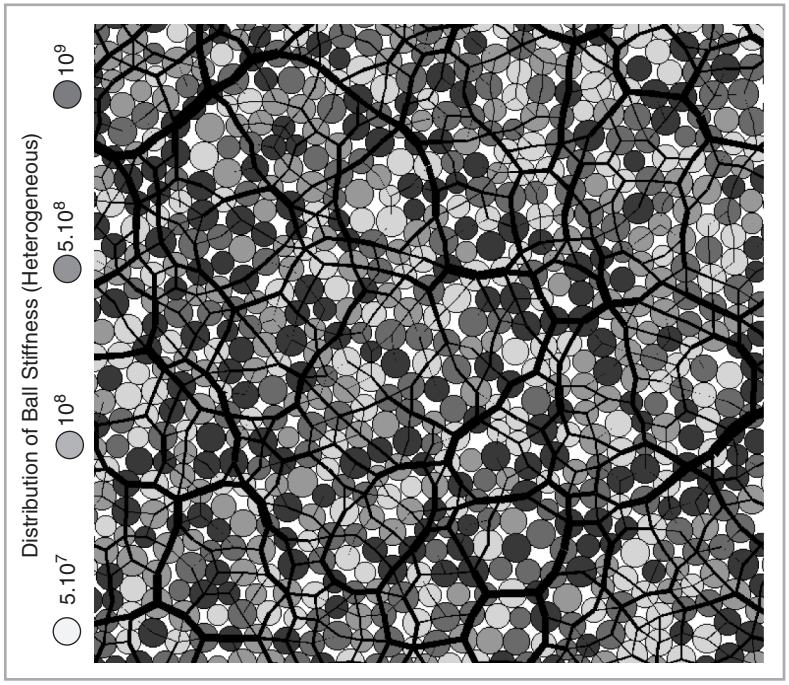

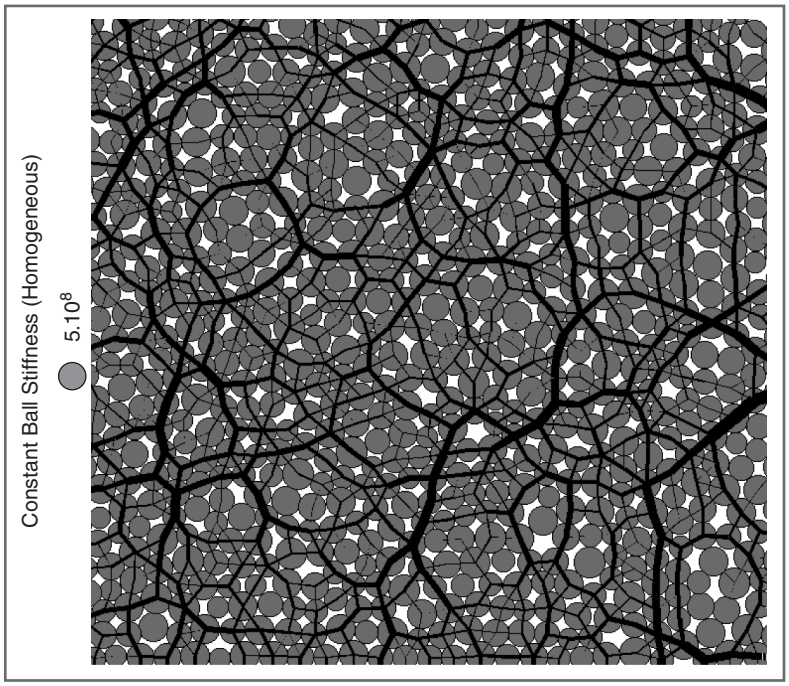

Figure 2.16a ▲

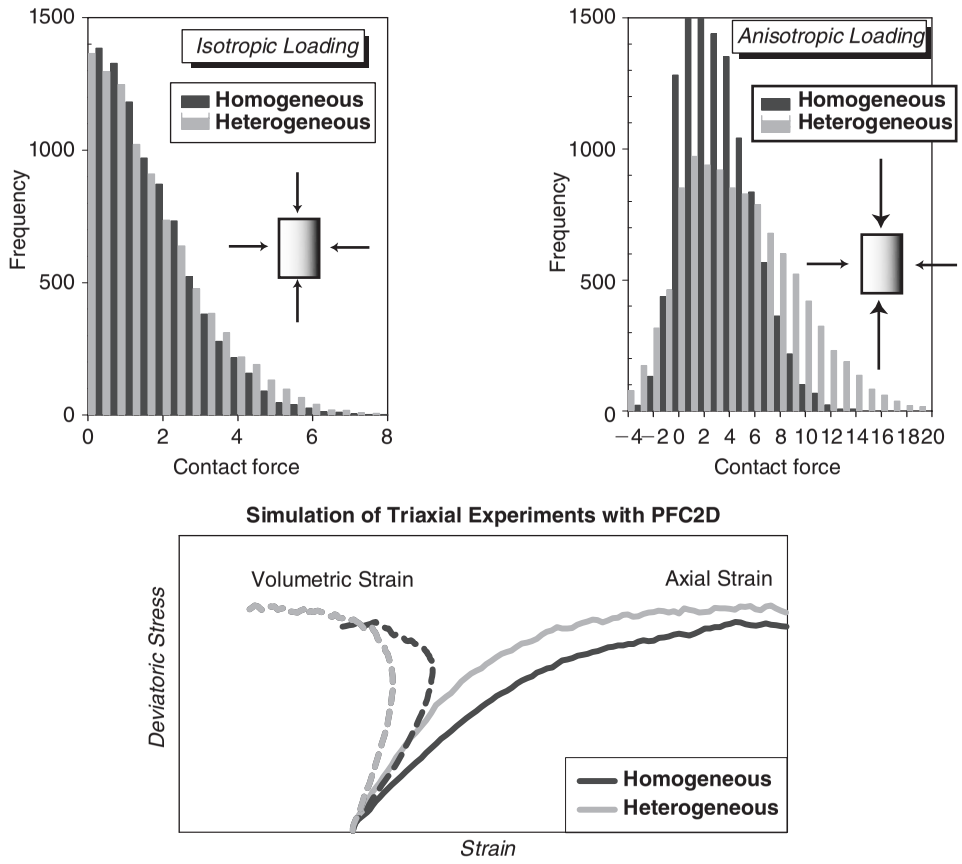

Figure 2.16b ► Localization and magnitude of chain forces at contacting particles for two random packings of disks. Homogeneous model (previous page left) has constant normal stiffness. Heterogeneous model (previous page right) has four classes of contact stiffnesses. The statistics of normal contact forces are shown (top) for two types of mechanical loading—isotropic and anisotropic. The loading curves for the simulated triaxial test are compared (bottom) for the homogeneous and heterogeneous models. PFC2D, Particle Flow Code 2-Dimensional. A color version of this figure is available online at book.elsevier.com / companions / 0123053552.

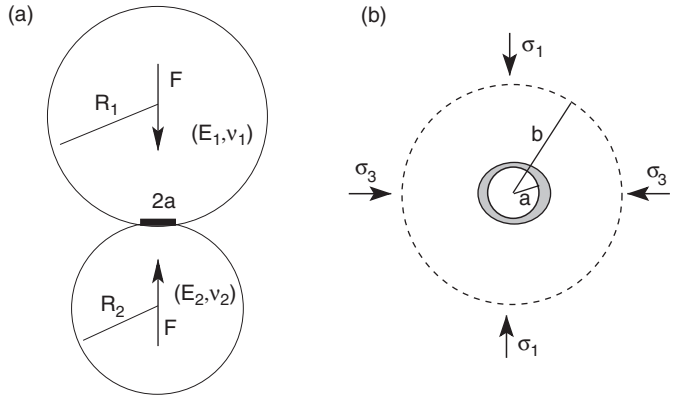

Figure 2.17 ► (*a*) Two spheres (of radii R_1 and R_2) in elastic contact under normal loading. (*b*) Plastic-pore-collapse model, with the onset of shear-enhanced compaction corresponding to initial yield at pore surface.

Assumptions in the derivation of the previous relations are that there is no adhesion or roughness at the contact, the size of the contact area is small compared with the radius of curvature of the spheres, and the strains are small enough to stay within the frame of the theory of elasticity. The local displacement in the direction of applied load is given by $\delta = a^2/R$, from which the normal stiffness $k_n = \partial F/\partial\delta$ can be calculated. The Hertzian contact theory provides also the stress evolution in the contact area, and it is found that the maximum hoop stress is located close to the circular external boundary of the contacting area. Therefore this region is likely to be the seed of failure processes associated with crack nucleation or propagation within the solid spheres. This result combined with a fracture mechanics criterion will be used in the following section to account for the onset of grain crushing in porous materials. Notice that other contact models are available that take into account additional features such as cementation and friction; for a review of those, one can refer to Mavko et al. (1998).

Hertzian Fracture Mechanics and Compaction in Porous Siliciclastic Rock

Both AE activity and microstructural studies on deformed rock samples consistently show that the critical pressure P^* is a manifestation of the onset of grain crushing and widespread microcracking within the granular structure. Therefore one would expect that the critical pressure is related to microstructural parameters and that one should use some basic principles of fracture mechanics to tackle this problem. The starting point will be to consider two spherical particles with radius R, elastically isotropic and homogeneous with Young modulus E and Poisson ratio ν. Initially, the two particles touch at a single point; no cementation effect is

considered at this point. When a force F normal to the contact is applied, the contact area widens and the Hertzian contact theory gives the radius a of the contact circle (see equation [2.4]). The maximum tensile stress is located at the circular boundary of the contacting area with magnitude

$$\sigma_t = \frac{(1-2\nu)}{2}\frac{F}{\pi a^2}. \tag{2.6}$$

Assuming that a crack of initial length c is located in the vicinity of the contact circle with $c \ll R$, the stress field at the tip of such a crack can be approximated by that of an edge crack in a semi-infinite medium: in such a case, the stress intensity factor in mode I (Lawn, 1993) is given by $K_1 = 1.12\sigma_t\,(\pi c)^{1/2}$. If the normal force increases such that K_1 reaches the fracture toughness (or critical stress intensity factor K_{1c}) of the solid material, the crack starts to propagate, and one can calculate by combining the previous equations the critical force needed for that to happen:

$$F_c = 17.84\frac{\left(1-\nu^2\right)^2}{E^2\,(1-2\nu)^3}\left(\frac{K_{1c}}{c^{1/2}}\right)^3 R^2. \tag{2.7}$$

There is the need now to relate the normal force acting on a single contact to the effective pressure applied at the macroscopic scale on the bulk rock. To do that, one has to provide a geometrical description of the granular assembly. Zhang et al. (1990a) proposed Brandt's (1955) random packing model of spheres with several sizes. With this assumption, the normal force F depends on the rock porosity ϕ, the radius of primary particles R, and the applied effective pressure P_e:

$$F = 8.1\phi^{3/2}R^2P_e, \tag{2.8}$$

and one can easily calculate the critical pressure P^* corresponding to the critical force F_c given above. To apply this result, one needs to know the size of preexisting flaws at the contact region between spherical particles. An additional reasonable assumption is to say that the flaw size scales like the particle size, in other words $c \propto R$. Introducing the flaw size ratio $\lambda = c/R$ we obtain the following relation for the critical pressure at the onset of grain crushing:

$$P^* = \Gamma\,(\phi R)^{-3/2}, \quad \text{with} \quad \Gamma = 2.2\frac{\left(1-\nu^2\right)^2}{E^2\,(1-2\nu)^3}K_{1c}^3\lambda^{-3/2} \tag{2.9}$$

According to this result (Zhang et al., 1990a), the critical pressure is controlled by specific parameters of the solid phase (elastic moduli E and ν, fracture toughness

K_{1c}), the flaw size ratio λ, and two parameters characterizing the granular assembly (porosity ϕ, grain radius R). Whereas it is always possible to calculate mean values for E, ν, and K_{1c} from a standard mineralogical composition, porosity and grain size are parameters that are highly variable in crustal rocks. Using such mean values and an estimate for the flaw size ratio λ, the model tells us that the critical pressure P^* should simply scale as $(\phi R)^{-3/2}$. The data in Figure 2.5 are consistent with such a dependence on the microstructure.

It should be noted that this Hertzian fracture model has a number of limitations. First, it does not explicitly include the influence of other microstructural parameters such as cementation and clay content. Second, it is essentially an effective-medium type of model that neglects the heterogeneity of elastic contact force. Third, the model considers only the initiation of microcracks at grain contact. It does not address the question of whether the subsequent crack propagation is stable (Lawn, 1998), nor does it account for the mechanical interaction among grain contacts. Notwithstanding these limitations, this micromechanical model for the onset of grain crushing seems to be relevant not only for a large number of siliciclastic rocks (including the synthetic sandstones discussed in a previous section) but also for unconsolidated materials, including sand and glass spheres (Figure 2.5). The straight line with slope $-3/2$ that best fits the data is consistent with a prefactor Γ equal to 1 in equation (2.9) when P^* is expressed in MPa and R in mm, an extremely easy relation to remember. It is then possible to estimate the critical pressure P^* from the knowledge of the bulk rock porosity and the mean grain size (in terms of equivalent grain radius). Nevertheless, as Figure 2.5 is a log-log scale plot, discrepancies with the former law can be large. This tells us that second-order effects, such as sorting, heterogeneity, anisotropy, and cementation, also may be important, but they are not taken into account in the first-order model presented here.

How can these relations be used? Starting from the knowledge of basic petrographic parameters like porosity and mean grain size for a given rock, it is possible to estimate the critical pressure P^* using equation (2.9). The normalized cap model provides additional information on the failure stress and rupture mode for any stress path in the following way. Consider, for example, a triaxial test conducted at an effective confining pressure $\sigma_3^{eff} = \sigma_3 - p$: the stress path in the normalized stress space is a straight line with slope 3 for normalized mean effective pressures larger than σ_3^{eff}/P^*. When the straight line hits the failure envelope given by equation (2.2), the stress state at failure can be derived by rescaling the coordinates of the intersection point by the factor P^*.

Equation (2.9) applies to Hertzian fracture due to normal loading. However, under nonhydrostatic loading shear-enhanced compaction arises from a combination of the normal loading induced by the mean stress and tangential loading induced by the deviatoric stresses. The tensile stress concentration at an impinging grain contact may be significantly enhanced by the tangential loading. The end-member case with a tangential force sufficiently high to overcome the frictional

resistance on the contact surface (characterized by the friction coefficient f) was analyzed by Hamilton and Goodman (1966), who showed that the stress concentration at the trailing end of the contact region is enhanced by a factor of $15.5f$. This is probably an upper bound on the tensile stress enhancement (Wong et al., 1997). The stress field and fracture mechanics of a partially slipped scenario were analyzed by Shah and Wong (1997). Their results show that the somewhat smaller enhancements in tensile stress and K_1 are still adequate to initiate grain crushing at mean stresses significantly lower than P^*, in agreement with the laboratory data on shear-enhanced compaction. Since the micromechanical analysis is quite involved, it is not straightforward to relate the results to the macroscopic yield cap.

The Hertzian fracture model can be modified to account for the chemical effect due to water. According to the Griffith (1920) theory, the mechanics of fracture in an ideally brittle solid is governed by the specific surface energy γ, such that equilibrium propagation of a crack occurs if the strain energy release rate G attains the critical value $G_c = 2\gamma$ (also called the fracture energy). As discussed in Chapter 1 this condition can equivalently be expressed in terms of the stress intensity factors K_1(Irwin, 1958; Lawn, 1993). In an elastic solid, extensile crack growth (in plane strain conditions) occurs if the stress intensity factor attains the critical value K_{1c} such that

$$G_c = \frac{(1-\nu^2)}{E} K_{1c}^2 = 2\gamma. \tag{2.10}$$

One of the earliest theories of chemistry in brittle fracture was that of Orowan (1944), who proposed that the environmental molecules lower the interface energy on entering the crack interface and adsorbing onto the walls in the cohesion–adhesion zone. While the decohesion of a solid body in vacuo is characterized by the specific surface energy γ, the separation of two solid half-bodies in a fluid environment is characterized by the solid–fluid interface energy γ'. For the environmentally susceptible system, equilibrium propagation of a tensile crack occurs if the strain energy release rate (or stress intensity factor) attains the critical value $G_c^{'}$(or $K_{1c}^{'}$) such that

$$G_c^{'} = \frac{(1-\nu^2)}{E} K_{1c}^{'2} = 2\gamma^{'}. \tag{2.11}$$

If $\gamma' < \gamma$, then adsorption occurs and the cohesion of the solid is lowered by the environmental interaction, with corresponding reduction in strength that is related to the ratio $\gamma'/\gamma = (K_{1c}^{'}/K_{1c})^2$. In equation (2.9), since environmental interaction is not expected to have insignificant impact on the elastic moduli, initial crack length, or porosity, the critical pressure in a saturated sample is expected to have a lower value that arises primarily from environmentally

induced reduction of the fracture toughness. This implies that in the Hertzian fracture model the water-weakening effect on grain crushing is described by $P^*_{wet}/P^*_{dry} = (\gamma'/\gamma)^{3/2} = (K'_{1c}/K_{1c})^3$ (Baud et al., 2000a). Hence hydrostatic data on grain crushing pressures of dry and wet samples can be used to infer the ratio γ'/γ. Baud et al. (2000a) showed that the water-weakening effect in the the Darley Dale, Gosford, and Boise sandstones can be explained by comparable values of this ratio (ranging from 0.83 to 0.89), while the water-weakening effect is almost negligible in Berea sandstone (with $\gamma'/\gamma = 0.97$). These relatively small reductions in fracture energy due to the presence of water are in agreement with limited fracture-mechanics data for silicate minerals and rocks (Atkinson and Meredith, 1987).

In carbonate rocks the limestone and chalk data suggest the operation of a similar mechanism. However, there are two intriguing features of the carbonate data that should be noted. First, the chemical effect seems to be sensitive to grain size. While appreciable weakening in the presence of water has been observed in limestones typically with grain size in the micrometer range, Rutter (1972) concluded that the chemical effect on failure in the relatively coarse-grained Carrara marble (with average grain size of 0.2 mm) was negligible. Second, the chemical effect is enhanced in carbonate rocks of higher porosity. While the strength is reduced by $\sim$30% in Solnhofen and Indiana limestone (Boozer et al., 1963; Rutter, 1974) in the presence of water, the corresponding reduction in chalk has been reported to be $>$50% in chalk (Risnes et al., 1996; Homand and Shao, 2000). Boozer et al. (1963) have suggested that if water - weakening arises from a reduction of the surface energy of calcite induced by the polar interaction between water and the grain surface, then the mechanism may also be coupled to the interaction of dislocations and point defects. Such a weakening effect through interaction at grain boundaries is likely to be greatest in rocks of high porosity and small grain size in which a large surface area will be exposed to the pore fluid (Rutter, 1972).

Plastic Pore Collapse and Compaction in Porous Carbonate Rocks

Baud et al. (2000b) suggested that since inelastic compaction in a porous carbonate rock is not dominated by grain-scale cracking, a more appropriate model for the micromechanics may be that of Curran and Carroll (1979), which appeals to plastic collapse of spherical pores. For a rock in which crystal plasticity processes (such as mechanical twinning and dislocation slip in calcite) are dominant, Curran and Carroll (1979) modeled the stress-induced compaction that arises from plastic collapse of isolated spherical pores. The applied stress field induces stress concentration in the vicinity of the spherical pore, and plastic flow occurs if the local stress field satisfies the von Mises yield criterion $\sqrt{J_2} = k = Y/\sqrt{3}$, where J_2 is the second invariant of the deviatoric stress tensor, and the parameters k and Y correspond to the plastic yield stresses for pure shear and uniaxial tension (or compression), respectively.

For hydrostatic loading this elastic-plastic model predicts that initial yield (corresponding to the onset of plastic collapse) occurs at the macroscopic critical pressure

$$P^* = \frac{2}{3}Y\left[1 - \frac{2\mu\phi}{2\mu + Y(1-\phi)}\right], \tag{2.12}$$

where μ is the shear modulus. As discussed earlier this model when applied to porous carbonate rock data would predict that the yield stresses (k and Y) decrease with increasing porosity (Figure 2.7b). For reference, the critical resolved shear stresses for various crystal plasticity mechanisms in calcite are also indicated in the figure. Hence one plausible interpretation of the carbonate rock data is that different crystal plasticity processes were activated in the two porosity ranges (Vajdova et al., in press) . On one hand, the relatively low yield stress values inferred for the porosity range of 15%–45% are comparable to the shear stresses required to activate e-twinning in calcite. On the other hand, in porosities <15%, the relatively high yield stresses are comparable to those associated with dislocation slip processes. Indeed, for the Solnhofen limestone with 3% porosity, Baud et al. (2000b) have suggested that since the von Mises requirement of five independent slip systems represents a necessary condition for macroscopic flow in the vicinity of a spherical pore, multiple slip systems (some of which are not favorably oriented) need to be activated at very high yield stresses.

Curran and Carroll (1979) also derived the critical condition for the onset of shear-enhanced compaction (Figure 2.17b). For a porous rock subjected to conventional triaxial compression, plastic yield initiates at the circular perimeter of the spherical pore that is parallel to σ_3 if the remotely applied stresses satisfy this condition:

$$9RP^2 + SP(3P - Q) + (U + V + 3W)(P - Q/3)^2 + 2WPQ = k^2 = Y^2/3, \tag{2.13}$$

where P is the mean stress and Q is the differential stress. The coefficients R, S, U, V, and W (which depend on the elastic moduli and the porosity) are given by Baud et al. (2000b) in their Appendix 1. If the elastic moduli are specified and the principal stresses are normalized with respect to Y, then a family of yield envelopes can be calculated using equation (2.13) for different values of initial porosity. The model predicts that the compactive yield stress at the onset of plastic pore collapse decreases with increasing mean stress and porosity. Figure 2.18 shows the Solnhofen limestone data for the onset of shear-enhanced compaction fitted to equation (2.13), assuming k = 563 MPa (or Y = 975 MPa). The experimental data describe a yield cap similar in shape to that predicted by the plastic-pore-collapse model.

For dislocation slip in calcite, the critical resolved shear stress for f-slip in calcite is 216 MPa and for r-slip it ranges from 145 to 185 MPa (Turner et al., 1954; Griggs et al., 1960). Although the inferred value of k in Figure 2.18 is

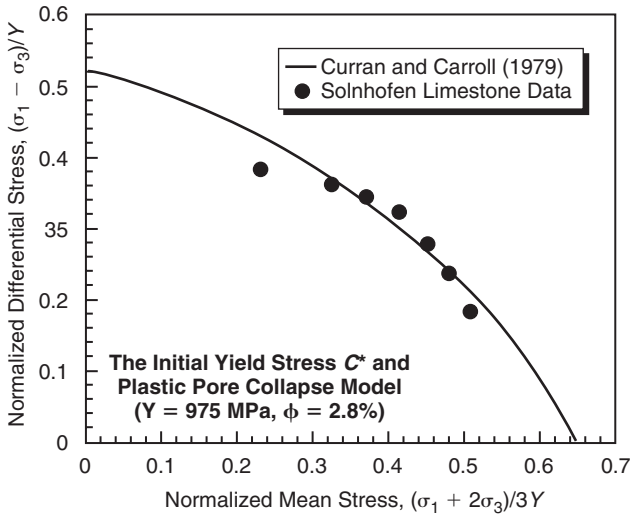

Figure 2.18 ► Comparison between the Solnhofen limestone data of Baud et al. (2000b) and Curran and Carroll's (1979) model, plotted in the P–Q stress space normalized by the yield stress taken as 975 MPa.

higher than these yield stresses measured for specific slip systems of calcite, Baud et al. (2000b) argued that it is likely that the macroscopic yield would involve a significantly higher stress level. Since the model requires homogeneous plastic flow to occur in the proximity of the pore surface, the von Mises requirement of five independent slip systems as a necessary condition for this type of macroscopic flow implies that multiple slip systems (some of which are not favorably oriented) need to be activated (Paterson, 1969, 1979). Compactive yield data for more porous carbonate rocks (Figure 2.11) are qualitatively similar to those for the relatively compact Solnhofen limestone, implying that the plastic-pore-collapse model is also applicable. However, the compactant deformation in a highly porous limestone or chalk may be dominated by the interplay of mechanical twinning and cataclasis, with minimal involvement of dislocation activity and a significantly lower yield stress (Vajdova et al., in press).

2.3.2 Microstructural Observations and Damage Evolution

Microscopy studies of experimentally and naturally deformed rock samples provide important information on several related questions. What are the geometric attributes of the pore space of a natural rock in a relatively undeformed state? The geometric complexity can significantly influence the stress concentration and

heterogeneity in response to an applied stress. It also may lead to a preferential flow path and channeling of fluid transport in response to a hydraulic gradient. How does damage accumulate and coalesce to culminate in macroscopic failure? Microscopy observations on deformed samples elucidate the mechanics of inelastic deformation and strain localization. To what extent is microstructure in naturally deformed samples reproduced in laboratory deformed samples? Establishing connection between the two allows one to have confidence in extrapolating laboratory observations and theoretical model to natural settings.

While our review will focus on microstructure in experimentally deformed samples, a few comments should be made on microscopy observations of naturally deformed samples. Many such observations have been made on localization features in fault zones (e.g., Antonellini et al., 1994; Fowles and Burley, 1994; Willemse et al., 1997; Shipton and Cowie, 2001). Snoke et al. (1998), Fisher et al. (1999), and Blenkinsop (2000) presented comprehensive reviews that include many excellent field examples of compactive cataclasis that corroborate the experimental deformation and theoretical models discussed in this chapter. It should be noted that field examples of grain fracturing can also be found in pitted pebble conglomerates (McEwen, 1981) and glacial sediments (Van der Meer, 1993; Hiemstra and van der Meer, 1997). In interpreting the microstructure induced by natural deformation a complication arises because microcracks from cataclastic deformation might have healed subsequently and their presence cannot be detected from aperture openings. Cathodoluminescence microscopy has become a useful tool for resolving such healed cracks (Lloyd and Hall, 1981; Laubach, 1997). Another complication arises because mechanical and chemical compactions may operate simultaneously and interact in a complicated manner (Gratier et al., 1999; Fisher et al., 1999).

To image the pore geometry and damage the first approach has usually been to use the optical microscope to examine thin sections. The scanning electron microscope (SEM) has proved to be very useful in studying the morphology of pores and cracks (Lloyd and Hall, 1981). Brace et al. (1972) introduced the procedure of ion-milling and attained a resolution of 0.02 μm of crack aperture. The acoustic microscope has also been used to delineate the cracks and mineralogical differences (Danburg and Yuhas, 1978; Briggs, 1992), and a resolution of about 1 μm can be obtained at a frequency of 1.6 GHz (Rodriguez-Rey et al., 1990).

Traditional microscopy techniques have the limitation that imaging is done in two dimensions only. Qualitative insights into the three-dimensional geometric complexity can be gained from SEM observations on pore casts. The pore space is first impregnated with acid-resistant epoxy (Pittman and Duschatko, 1970; Wardlaw, 1976) or Wood's metal (Dullien and Dhawan, 1975; Myer et al., 1992; Darot and Reuschle, 1999), and then the solid grains are dissolved with acid. However, it is difficult to characterize quantitatively the three-dimensional pore structure. Interpolation of two-dimensional images on serial sections can provide such data (Koplik et al., 1984), but the procedure is very tedious to implement.

There have been significant advances in several three-dimensional imaging techniques.

- X-ray computer tomography (Wellington and Vinegar, 1987; Raynaud et al., 1989; Kawakata et al., 1999) is used to characterize the spatial distribution of porosity at a resolution of about 0.5 mm.
- Nuclear magnetic resonance technique (Fukushima, 1999; Osment et al., 1990) with a resolution of about 25 μm has been used to characterize the pore geometry and image the flow of fluid (Kenyon, 1992; Geraud et al., 1995; Kleinberg, 1999).
- Even higher resolution (of 1 to 10 μm) is available from synchrotron computed microtomography (Flannery et al., 1987) of cylindrical samples of porous rock with diameter of 5 mm or larger (Spanne et al., 1994; Auzerais et al., 1996; Coker et al., 1996; Coles, 1999).
- The finest resolution ($\sim$0.2 μm) is attained by the use of the laser scanning confocal microscope (LSCM) on rock samples impregnated with an epoxy that has been doped with a fluorochrom (Fredrich et al., 1995; Montoto et al., 1995; Petford et al., 1999; Menéndez et al., 2001). In a porous sandstone, a penetration depth of about 250 μm can be achieved before significant image degradation is apparent (Fredrich, 1999). Yu et al. (2002) used holographic laser imaging to probe a sandstone sample down to a depth of $\approx$400 μm, with a relatively coarse resolution of $\approx$10 μm.

Characterization of Stress-Induced Microstructure

The damage is characterized by comparing the microstructure in a stressed sample with that in an unstressed sample. In unstressed rock samples, the pore space can be conveniently divided into microcracks and almost equant pores. Microcracks are the main source of porosity and permeability in rocks of low porosity, and their morphology has been reviewed by Paterson (1978) and Kranz (1983). In rocks of high porosity, the initial structure of the pore space also includes numerous tubular pores, typically located at interfaces between several grains. Here we will summarize the stress-induced microstructure, focusing on the more extensive and systematic observations in porous sandstones. Microstructural studies of damage in carbonate rocks have not been as comprehensive, and we do not intend to review the data here.

Figures 2.19 and 2.20 show three-dimensional perspective views of the pore space geometry in unstressed samples of Bentheim and Rothbach sandstones, with average porosities of 23% and 22%, respectively. These images are obtained by volume rendering starting from a series of two-dimensional micrographs obtained at different depths using the LSCM (Menéndez et al., 2001). They characterized the complexity of the pore space in sandstones in terms of connectivity, pore shape, and surface roughness. The complex geometry of intergranular pores is often

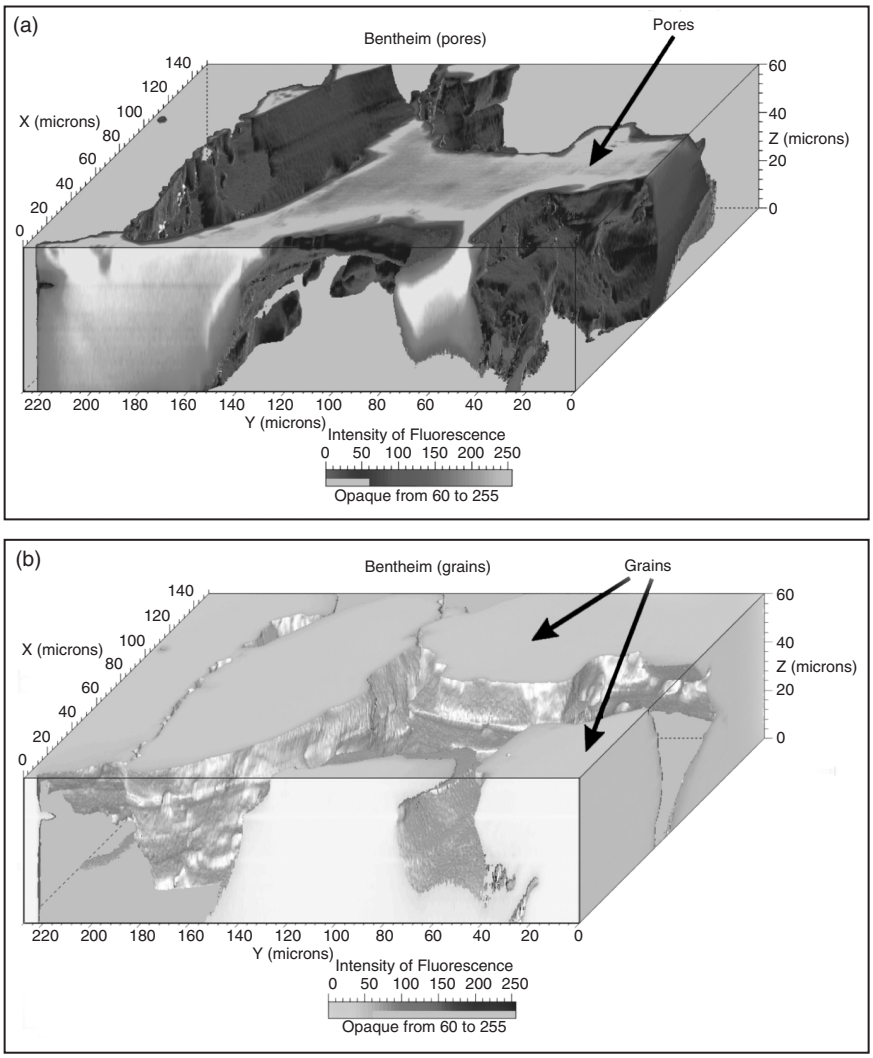

Figure 2.19 ► Three-dimensional reconstruction of the pore space in Bentheim sandstone from a laser scanning confocal microscopy (LSCM) study. The color scale is related to the intensity of fluorescence captured by the LSCM. The data can be presented in two different ways: (a) the pores are represented by the opaque phase while the grains are transparent; (b) the pores are represented as transparent voids between solid grains. Notice the complex grain-to-grain contact geometry on the left, and the generally smooth interface between grains and pores. A color version of this figure is available online at book.elsevier.com / companions / 0123053552.

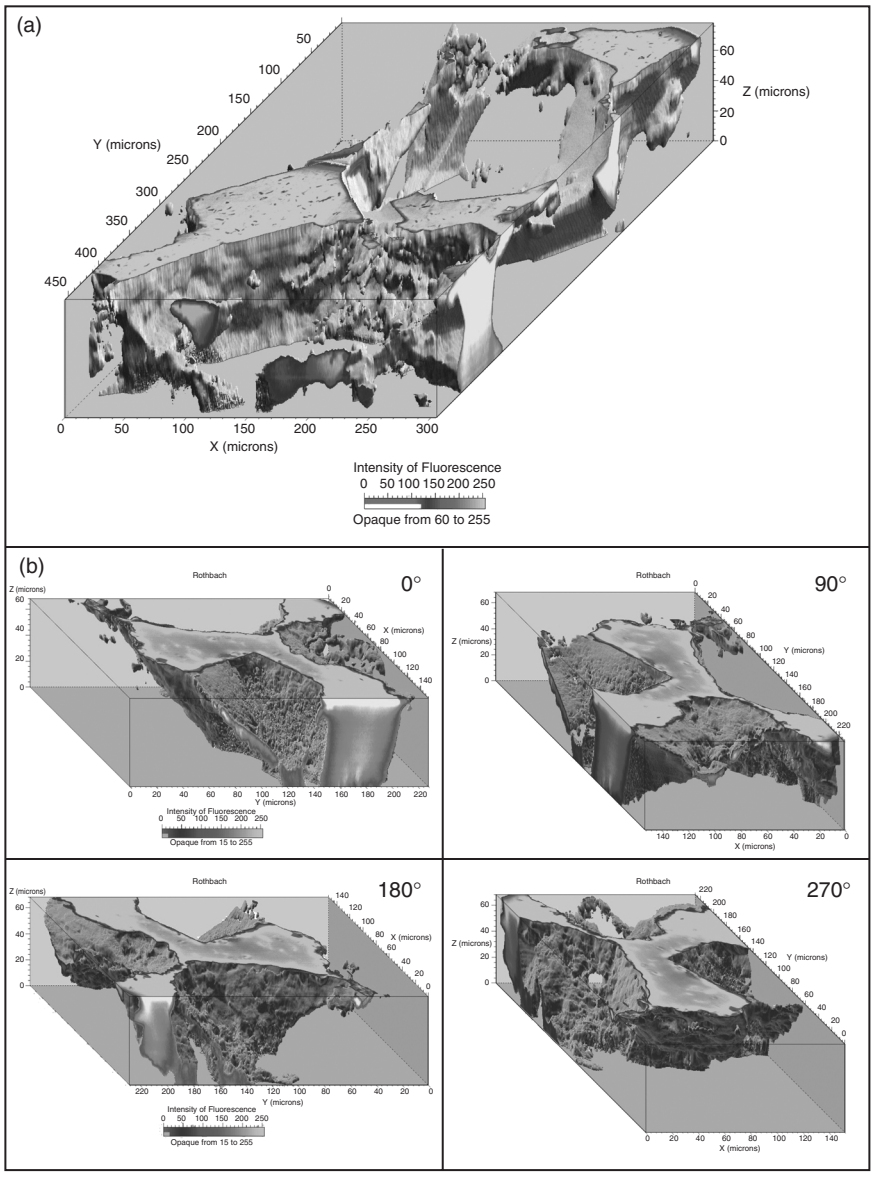

Figure 2.20 ► (a) Three-dimensional reconstruction of the pore space in Bentheim sandstone. With a larger field of view than Figure 2.19, the complex topology of the pore network is highlighted here. (b) A set of four different views from a three-dimensional reconstruction on Rothbach sandstone. The rendered volume is rotated by 90° around the z-axis in each view. The pore space coordination number equals 3. Also notice the pore-to-throats connections and the fine-scale surface roughness due to the presence of clays coating the grain surfaces. A color version of this figure is available online at book.elsevier.com / companions / 0123053552.

approximated by tubular shapes. Analysis of synchrotron X-ray tomographic data of the Fontainebleau sandstone indicates that the lengths of the tubular pores are comparable to the average grain size, and there is an overall decrease in these lengths with increasing porosity (Lindquist et al., 2000). With decreasing porosity and increasing cementation, there is an overall decrease of coordination number and loss of connectivity (Fredrich, 1999). While the geometric attributes and connectivity of the tubular pores influence significantly the elastic and transport properties, they are not as important as the microcracks in the development of brittle failure.

Figure 2.21a shows a SEM micrograph on unstressed Berea sandstone with initial porosity of 21% (Menéndez et al., 2001). For the stressed samples, the effect of hydrostatic compaction is most evident in samples that have been loaded

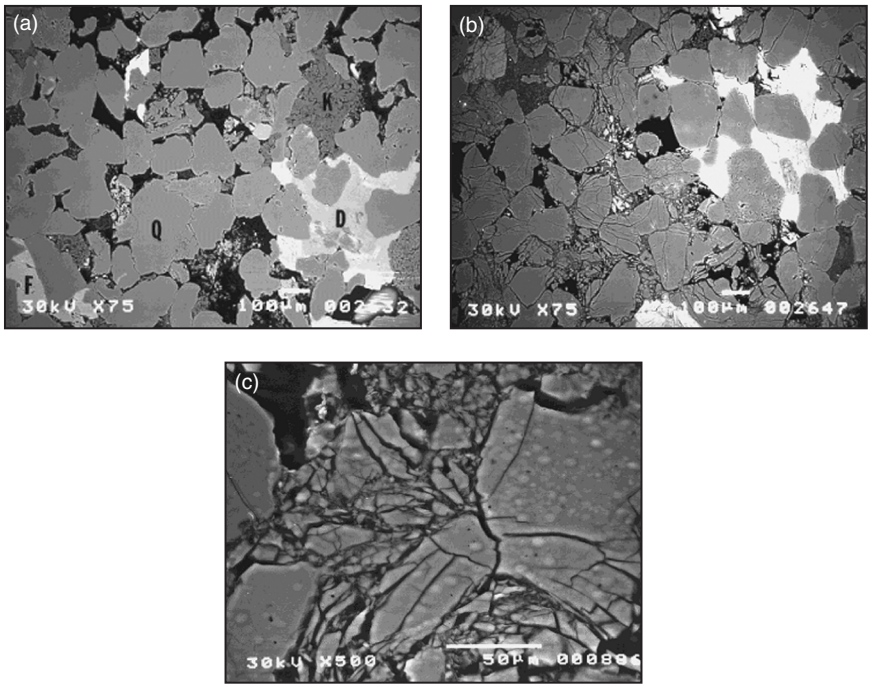

Figure 2.21 ► (*a*) SEM micrograph of an unstressed sample of Berea sandstone. The main mineralogical components are indicated: quartz (Q), kaolinite (K), and potassium feldspar (F). The lighter phase is the dolomite cement (D). (b) Grain crushing and pore collapse observed in a Berea sandstone sample that was hydrostatically compacted to beyond the critical effective pressure P^*. Note that the cracking is less intense in the vicinity of the carbonate cements (the lighter phases). (c) Details of intragranular Hertzian fractures emanating from contacts where grains impinge on one another, as observed in the same sample. The scale bars for (a) and (b) are 100 μm and for (c) 50 μm long.

to beyond the critical pressure P^*. As illustrated in Figure 2.21b grain crushing and pore collapse are pervasive in the hydrostatically compacted Berea sandstone sample. The spatial distribution of damage is quite heterogeneous, with the relatively intact grains commonly located in the vicinity of cemented contacts. The grain crushing process arises from extensive cracking that initiated from contacts between impinging grains (Figure 2.21c), in a manner analogous to the Hertzian fracture model previously discussed.

Figure 2.22 illustrates the damage evolution in sandstone during dilatant failure and shear localization in the Rothbach sandstone (Bésuelle et al., 2003). The micromechanics of brittle faulting has been investigated quite thoroughly (Menéndez et al., 2001; Mair et al., 2000; Wu et al., 2000; Bésuelle et al., 2000; El Bied et al., 2002), and the related microstructural development will be detailed in Chapter 4. Here we will focus on the damage from compactive failure. The damage structure associated with shear-enhanced compaction and cataclastic flow is illustrated by the observations of Wu et al. (2000) on the Darley Dale sandstone (with initial porosity of 13%). For reference, a SEM micrograph of the undeformed sample is shown in Figure 2.23a. Some grain boundaries were observed to be partially cracked, and relatively short intragranular cracks were located along

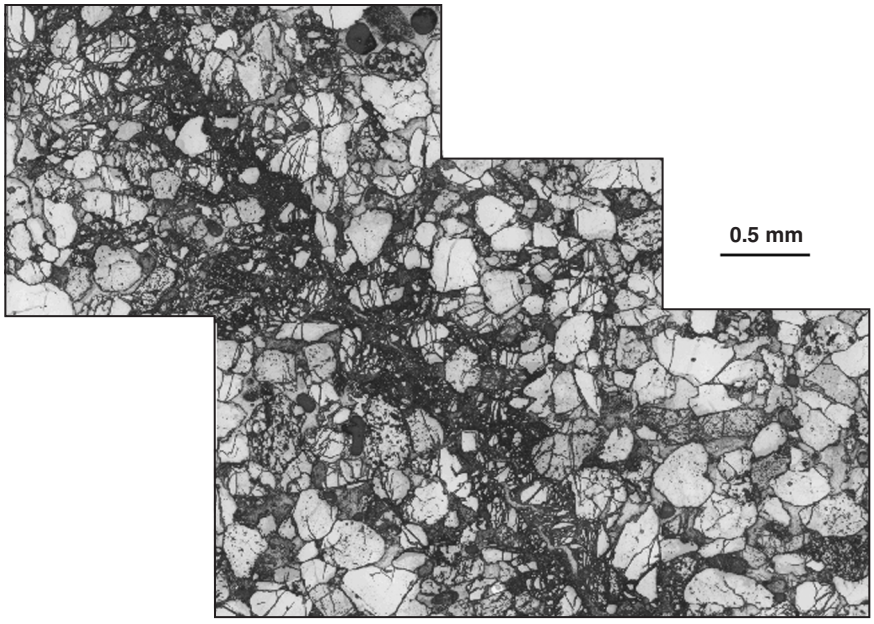

Figure 2.22 ► Mosaic of optical (reflection) micrographs showing part of the shear band that developed in a Rothbach sandstone sample deformed at an effective pressure of 20 MPa to the post-peak stage. Principal stress σ_1 was along the axial direction. A color version of this figure is available online at book.elsevier.com / companions / 0123053552.

cleavages of the feldspar grains. In a sample that had been deformed to just beyond the onset of shear-enhanced compaction, the development of Hertzian fractures is manifested by isolated clusters of intragranular cracks radiating from grain contacts (Figure 2.23b). With the further development of shear-enhanced compaction a larger number of crushed grains associated with intense intragranular cracking were observed in a sample that had been deformed to ≈9.5% of axial strain (Figure 2.23c). Many of the pores collapsed and the pore space was filled with comminuted particles (Figure 2.23d). The three-dimensional complexity of the damage is revealed by the LSCM images shown in Figure 2.24 and 2.25. In Figure 2.24a a subset of the micrographs scanned on the LSCM is shown, from which a three-dimensional reconstruction of the pore space is built in Figure 2.24b. This

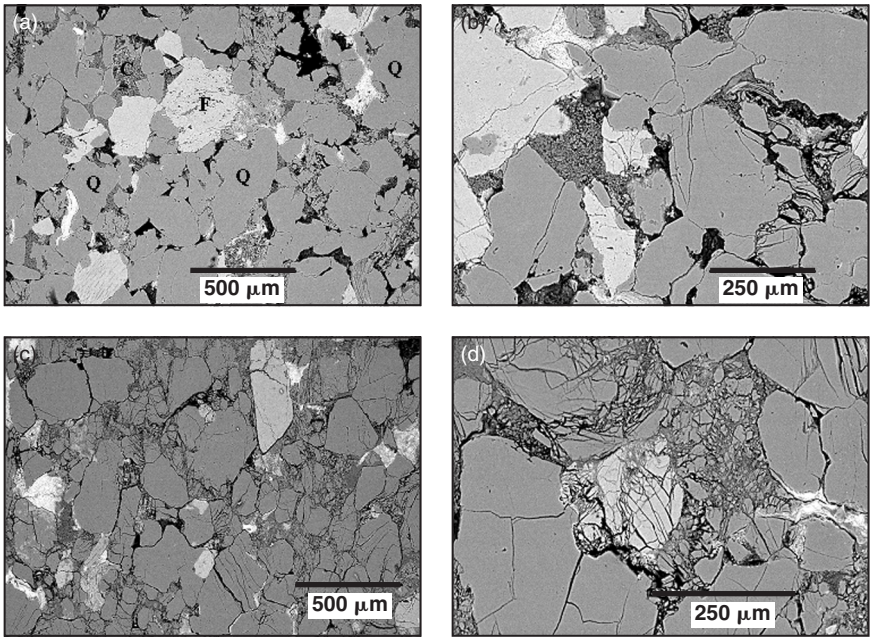

Figure 2.23 ► Scanning electron micrographs of unstressed and deformed samples of Darley Dale sandstone. (a) In an unstressed sample, the main mineralogical components are indicated: quartz (Q), clay (C) and feldspar (F). (b) Onset of grain crushing observed in a sample (WD1) that was triaxially compacted to just beyond the compactive yield stress C^* at effective pressure of 200 MPa. (c) Extensive development of grain crushing and pore collapse as observed in a shear-compacted sample (WD3) under relatively low magnification. The sample was deformed to well beyond C^* at effective pressure of 200 MPa (to a maximum axial strain of 9.5%). (d) Details of (c) revealed at higher magnification. The σ_1 direction is vertical in these micrographs. A color version of this figure is available online at book.elsevier.com / companions / 0123053552.

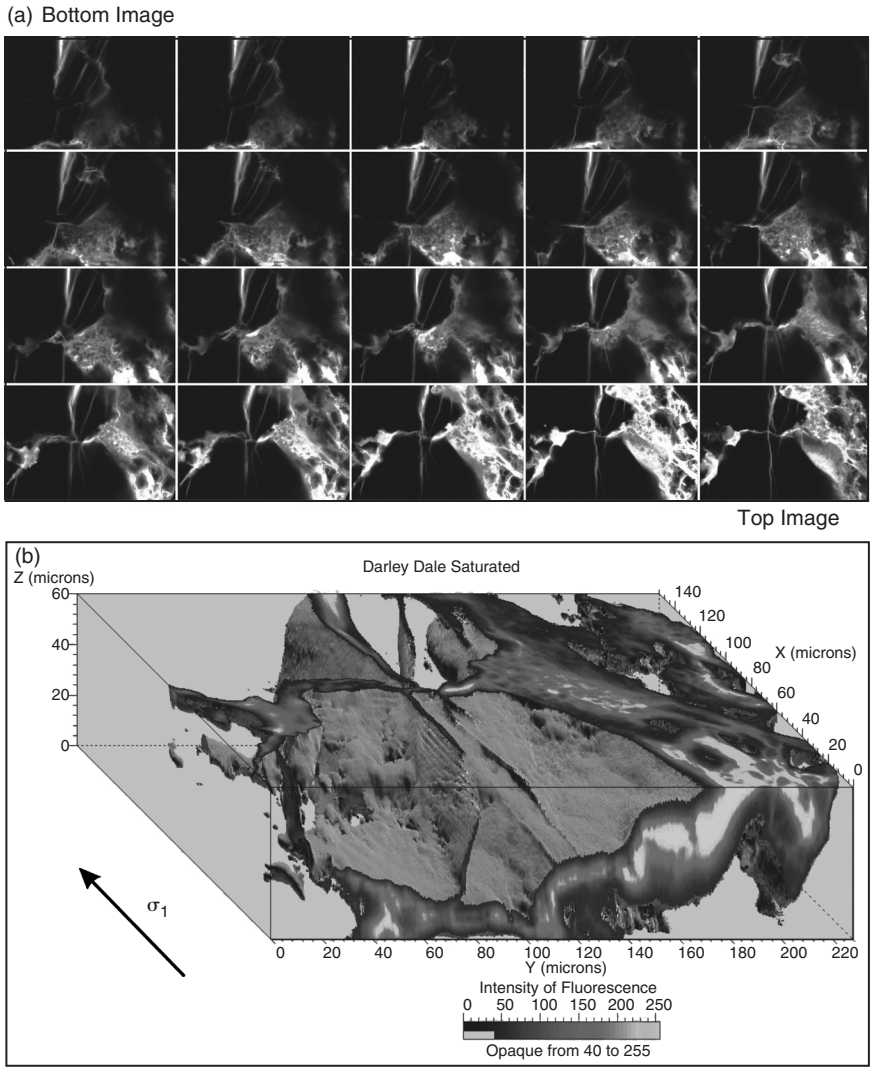

Figure 2.24 ► (a) A subset of the stack of micrographs used in the reconstruction of (b). Notice the typical Hertzian fractures emanating from the contact between two grains. (b) Three-dimensional LSCM reconstruction of the pore and crack network in a Darley Dale sandstone sample deformed to beyond C^* at effective pressure of 200 MPa (to a maximum axial strain of about 5%). A color version of this figure is available online at book.elsevier.com / companions / 0123053552..

example nicely illustrates the development of Hertzian fractures at the contact between two adjacent grains in a stressed sample of Darley Dale sandstone. Figure 2.25 gives two more examples on stressed samples of Darley Dale sandstone,

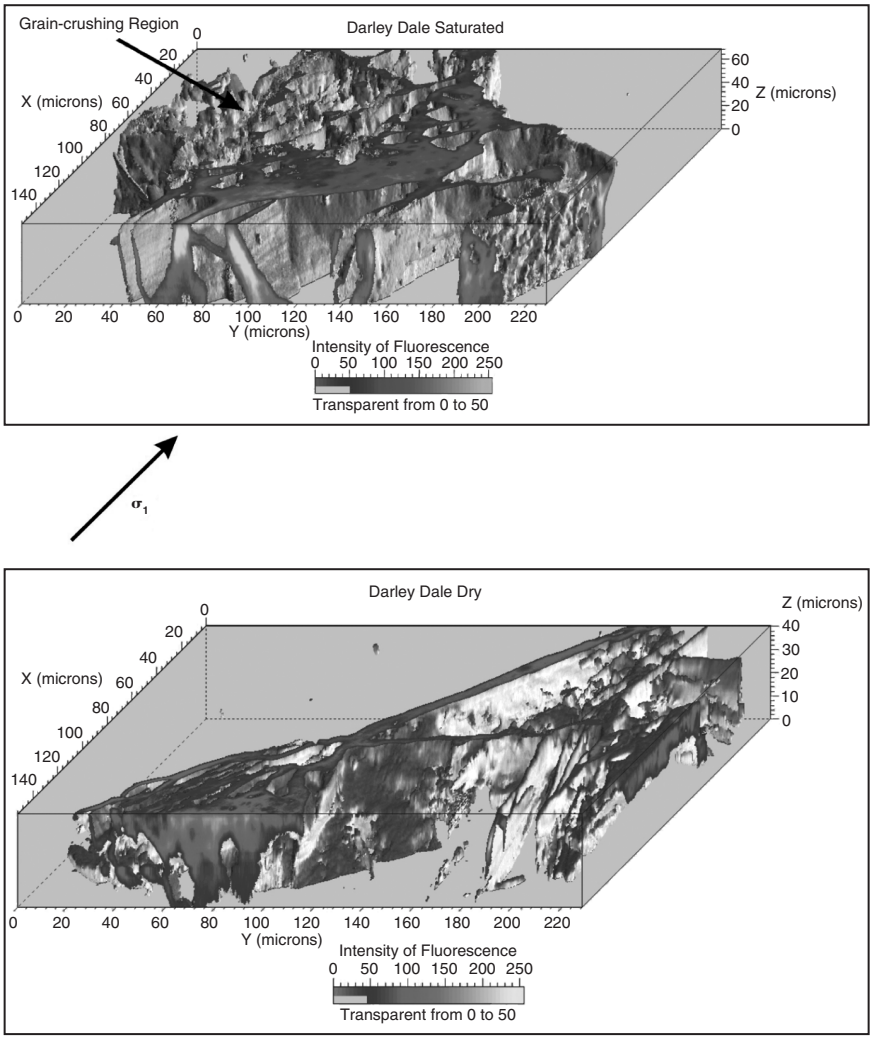

Figure 2.25 ► Two examples of three-dimensional LSCM reconstructions on shear-compacted Darley Dale sandstone. The deformation history is similar to the sample shown in the previous figure. Notice the preferred orientation of cracks in the direction of σ_1. The numerous small "holes" between the cracks correspond to two small fragments of grains that fill the pores when grain crushing and comminution take place. A color version of this figure is available online at book.elsevier.com / companions / 0123053552.

in which one can observe the preferred orientation of the cracks in a direction parallel to the maximum compressive stress and the typical features associated with pore collapse, grain crushing, and comminution.

Damage Evolution and Failure Mode

While such microstructural observations elucidate the damage mechanisms, a deeper understanding of compactive failure and strain localization necessitates a quantification of the damage accumulation and spatial evolution. Stereological and AE measurements can be used to characterize quantitatively the damage. A standard stereological technique is to count the number of crack intersections using a test array of regularly spaced parallel lines (Underwood, 1970; Russ, 1986). To characterize the stress-induced anisotropy in an axisymmetrically compressed sample, measurements are made in two orthogonal directions, parallel and perpendicular to σ_1, respectively. If the linear intercept densities (number of crack intersections per unit length) for the arrays oriented parallel and perpendicular to σ_1 are denoted $P_L^{\parallel}$ and $P_L^{\perp}$, respectively, then the crack surface area per unit volume S_V is given by

$$S_V = \frac{\pi}{2} P_L^{\perp} + \left(2 - \frac{\pi}{2}\right) P_L^{\parallel} \tag{2.14}$$

and the stress-induced anistropy in crack density can be characterized by the parameter

$$\Omega_{23} = \frac{P_L^{\perp} - P_L^{\parallel}}{P_L^{\perp} + (4/\pi - 1) P_L^{\parallel}} , \tag{2.15}$$

which represents the ratio between the surface area of the cracks parallel to σ_1 and the total crack surface area.

If the area of a deformed sample is subdivided into smaller elemental areas, then stereological measurements on each elemental area can be juxtaposed to map out the spatial evolution of damage. Wu et al. (2000) obtained such a set of refined stereological data for Darley Dale sandstone. For each sample a square area of 11×11 mm^2 centrally located in a thin section is subdivided into 11×11 elemental domains, each of which has an area of 1×1 mm^2. In each elemental area stereological measurements were performed with a test array of 10 parallel lines spaced at 0.1 mm (about 1/3 of the average grain size) apart. Contour plots of the stereological measurements of $P_L^{\parallel}$ and $P_L^{\perp}$ in the 121 elemental areas are shown in Figure 2.26. The stereological data for the unstressed and two deformed samples show that the overall damage increased progressively with the development of shear-enhanced compaction and strain hardening. While the damage seems to become somewhat anisotropic and more clustered in the highly deformed samples, shear localization is absent even in the sample that has accumulated an axial strain of 9.5%.

There is a strong correlation among the mean crack density (given by the arithmetical mean of the 121 stereological measurements for each sample), the axial strain, and AE activity (Figure 2.27). There is also an approximately linear relation between the average crack density and axial strain (Wu et al., 2000). It should be noted that more refined measurements of the spatial distribution

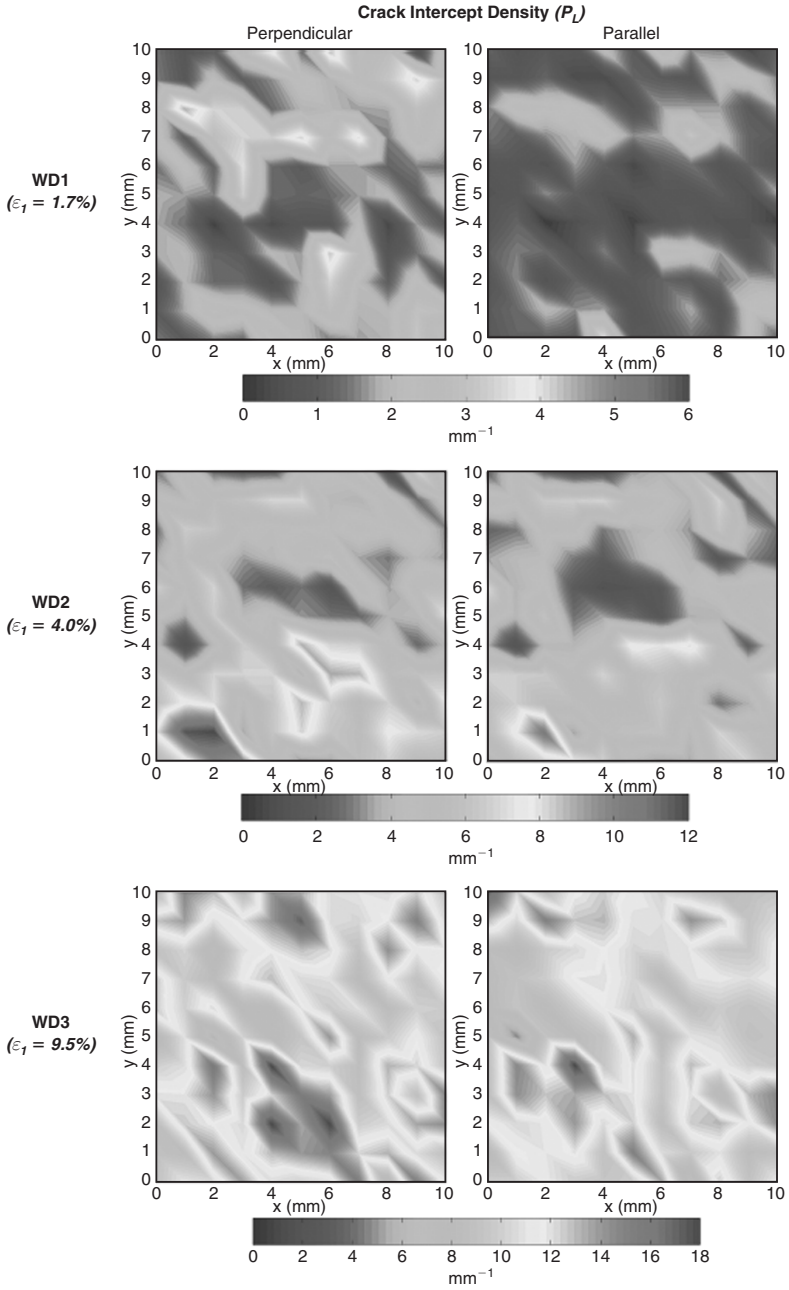

Figure 2.26 ► Spatial distribution of crack intercept densities measured perpendicular and parallel to σ_1 in three Darley Dale sandstone samples deformed at effective pressure of 200 MPa to axial strains of 1.7%, 4.0%, and 9.5%, respectively. A color version of this figure is available online at book.elsevier.com / companions / 0123053552.

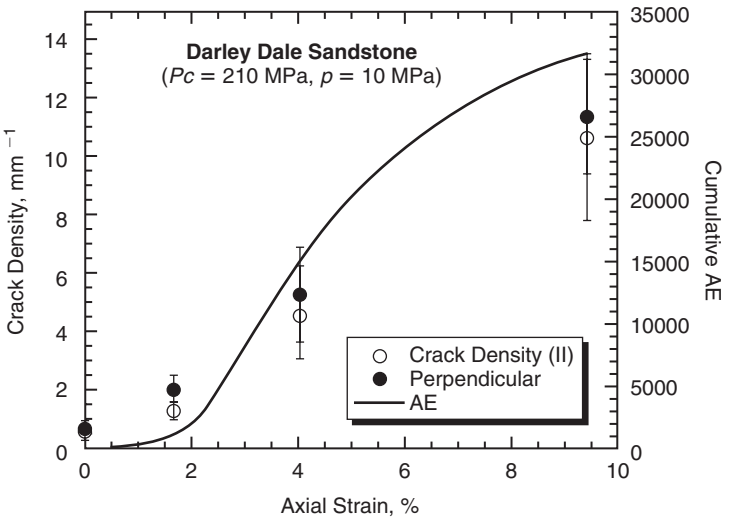

Figure 2.27 ► Correlation between crack densities and AE activity in the shear-compacted samples of Darley Dale sandstone. The crack intercept densities measured perpendicular and parallel to σ_1 are shown as solid and open symbols, respectively. The cumulative AE count is shown as continuous curve. P_c is confining pressure and P is pore pressure.

and focal mechanisms of AE events can also be performed. We will not discuss this topic here since a detailed review of such AE data is presented in Chapter 4.

Since dilatancy is generally observed as a precursor to brittle faulting and the development of shear localization, attention has focused on how localized failure develops in a dilatant rock. However, some geologic observations (Mollema and Antonellini, 1996) and reassessment of bifurcation theory (Chapter 5) have indicated that strain localization may be pervasive in a compactant porous rock. Systematic microstructural characterization demonstrates that such compaction localization phenomena are quite common in porous sandstones (DiGiovanni et al., 2000; Klein et al., 2001; Wong et al., 2001; Bésuelle et al., 2003, 2000), and they are generally associated with stress states in the transitional regime from brittle faulting to cataclastic ductile flow(Wong et al., 2001). While compaction and damage are usually delocalized in sandstone samples deformed under relatively high confinement (Figure 2.26), complex localized failure may occur when the sandstone is deformed in relatively low confinement.

Such a transition of failure mode in the Darley Dale sandstone is illustrated in Figure 2.28. While the stereological data in Figure 2.26 are for a sample deformed at effective pressure of 200 MPa, the data in Figure 2.28 are for four samples deformed at effective pressures of 80, 90, 95, and 110 MPa. The deformation and

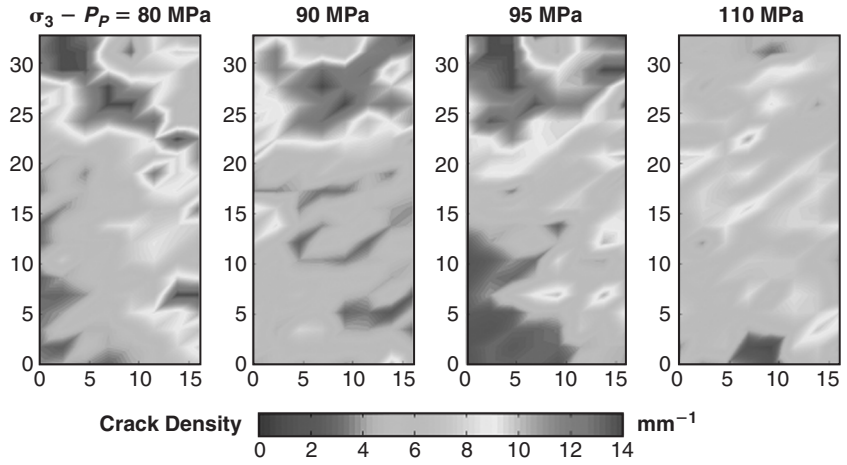

Figure 2.28 ► Spatial distribution of damage in Darley Dale sandstone samples deformed to just beyond the onset of shear-enhanced compaction (to axial strains as indicated). The saturated samples were deformed at pore pressure of 10 MPa and effective pressures as indicated. The maximum axial strains were 3.0% (at 80 MPa), 2.7% (at 90 MPa), 3.7% (at 95 MPa), and 3.6% (at 110 MPa). Principal stress σ_1 was along the axial direction. The spatial scales of the samples are in millimeters, and the crack density is specific crack surface area per unit volume inferred from stereological measurements. A color version of this figure is available online at book.elsevier.com / companions / 0123053552.

failure in the four samples were all accompanied by shear-enhanced compaction. Equation (2.14) was used to calculated the specific crack surface from the stereological data. Development of an elongate, connected cluster of anomalous damage that cuts through the sample can be considered as a proxy for localized failure.

- At 80 MPa, a shear band developed at $\sim 45^o$ in the failed sample. Although not included in Figure 2.28, a dilatant sample that failed at a lower confinement of 10 MPa was observed to have developed a shear band at $\sim 30^o$ (Wong et al., 1997).
- When the effective pressure was increased to 90 MPa and 95 MPa, shear and diffuse compaction bands at relatively high angles up to 90^o were observed (Figure 2.28). These bands often developed near one end of the sample.
- At 110 MPa the clusters of damage became delocalized, with a ductile failure mode analogous to that at 200 MPa (Figure 2.26).

Synthesizing their data for three sandstones and other published data (Olsson and Holcomb, 2000; DiGiovanni et al., 2000), Wong et al. (2001) concluded that compaction localization can develop in sandstones with porosities ranging from 13% to 28%, manifested by a spectrum of failure modes and geometric attributes. While

localization developed as high-angle shear bands or diffuse compaction bands in the Darley Dale sandstone (Figure 2.28) and Castlegate sandstone (DiGiovanni et al., 2000), subparallel arrays of discrete bands associated with intensive comminution and porosity reduction (corresponding to the dark bands perpendicular to σ_1 in the transmission optical micrographs) were observed in failed samples of the Bentheim sandstone at confining pressures from 120 to 300 MPa (Figure 2.29). The stress–strain curve typically shows an overall strain hardening trend that is punctuated by episodic stress drops (Klein et al., 2001). The number of discrete compaction bands was observed to increase with the cumulative number of stress drops. Such mechanical and microstructural attributes of the Bentheim sandstone are very similar to those of honeycombs (Papka and Kyriakides, 1999), metal foams (Bastawros et al., 2000), and ice during the I→II transformation Kirby et al. (1992) that have failed by development of compaction bands.

Using AE locations, Olsson and Holcomb (2000) mapped out in detail the spatial evolution of damage during compaction band formation. Baud et al. in press also demonstrated that the development of compaction bands is associated with distinct surges in AE activity, and in some cases the bands may initiate as discrete entities that subsequently coalesce to develop a mosaic of diffuse bands,as illustrated in Figure 2.30 for a Berea sandstone sample. The mechanics of compaction localization is being actively investigated in a number of laboratories, and the theoretical analysis of such phenomena is addressed in Chapter 5.

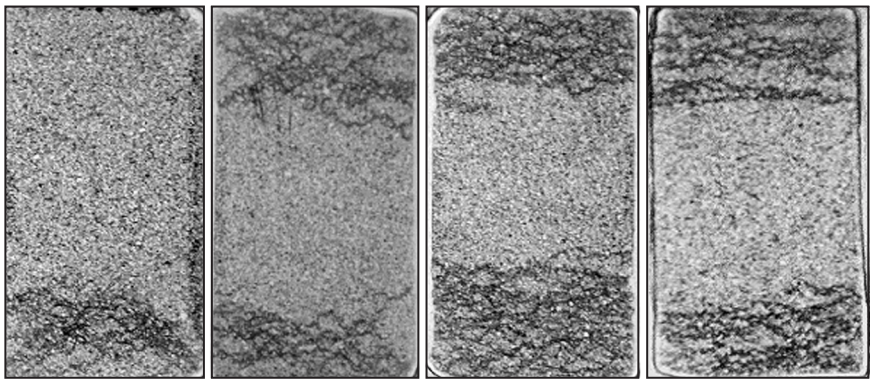

Figure 2.29 ► Transmission optical micrographs of Bentheim sandstone samples deformed to just beyond the onset of shear-enhanced compaction (to axial strains as indicated). The nominally dry samples were deformed at confining pressures as indicated. The maximum axial strains were 2.8% (at 90 MPa), 3.5% (at 120 MPa), 4.0% (at 180 MPa), and 3.0% (at 300 MPa). The dark bands are associated with significant compaction and damage. The width of each thin section is ≈18 mm. Principal stress σ_1 was along the axial direction.

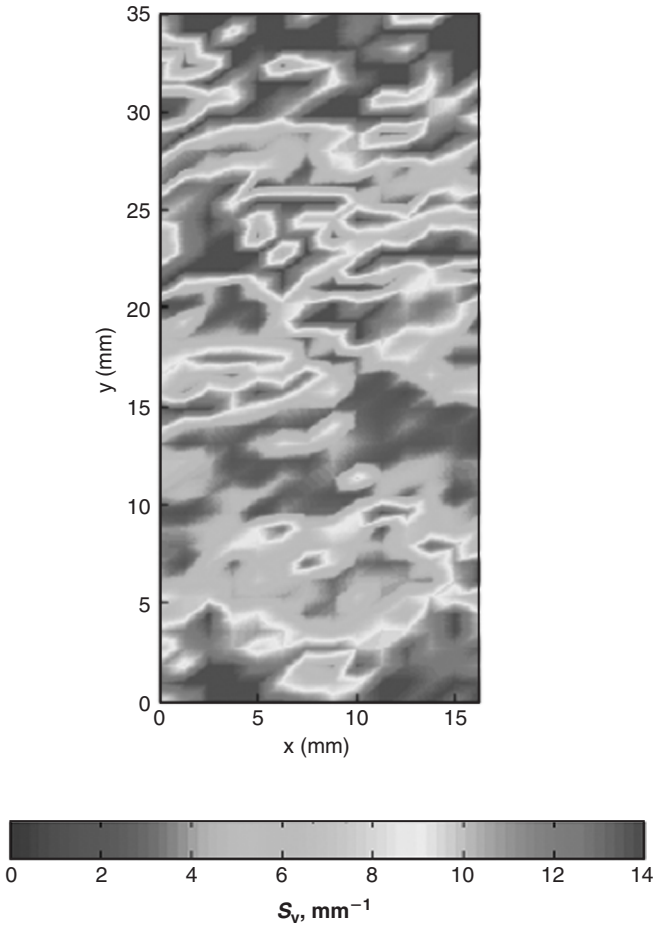

Figure 2.30 ► Spatial distribution of damage in a Berea sandstone sample reveals a mosaic of diffuse compaction bands. Principal stress σ_1 was along the axial direction. The complex pattern of compaction localization was observed by Baud et al. in press in a sample deformed to beyond the onset of shear-enhanced compaction at effective pressure of 200 MPa. A color version of this figure is available online at book.elsevier.com / companions / 0123053552.

Bibliography

Antonellini, M., Aydin, A. and Pollard, D.D. Microstructure of deformation bands in porous sandstones at Arches National Park, Utah. *J. Struct. Geol.* 16: 941–959, 1994.

Atkinson, B.K., and Meredith, P.G. Experimental fracture mechanics data for rocks and minerals. In *Fracture Mechanics of Rock,* Atkinson, B.K., ed., pp. 477–525. Academic Press, London, 1987.

Auzerais, F.M., Dunsmuir, J., Ferreol, B.B., Martys, N., Olson, J., Ramakrishnan, T.S., Rothman, D.H., and Schwartz, L.M. Transport in sandstone: A study based on three dimensional microtomography. *Geophys. Res. Lett.* 23: 705–708, 1996.

Bastawros, A.-F., Bart-Smith, H., and Evans, A.G, Experimental analysis of deformation mechanisms in a closed-cell aluminum alloy foam. *J. Mech. Phys. Solids* 48: 301–322, 2000.

Baud, P., Zhu, W., and Wong, T.-f. Failure mode and weakening effect of water on sandstone. *J. Geophys. Res.* 105: 16371–16390, 2000a.

Baud, P., Schubnel, A., and Wong, T.-f. Dilatancy, compaction and failure mode in Solnhofen limestone. *J. Geophys. Res.* 195: 19289–19303, 2000b.

Baud, P., Klein, E., and Wong, T.-f. Compaction localization in porous sandstones: Spatial evolution of damage and acoustic emission activity. *J. Struct. Geol.,* in press.

Bésuelle, P., Desrues, J., and Raynaud, S. Experimental characterisation of the localisation phenomenon inside a Vosges sandstone in a triaxial cell. *Int. J. Rock Mech. Min. Sci.* 37: 1223–1237, 2000.

Bésuelle, P., Baud, P., and Wong, T.-f. Failure mode and spatial distribution of damage in Rothbach sandstone in the brittle-ductile transition. *Pure Appl. Geophys.* 160, 851–868, 2003.

Berner, R.A. *Early Diagenesis*. Princeton University Press, Princeton, 1980.

Biot, M.A. General theory of three dimensional consolidation. *J. App. Phys.* 12: 155–164, 1941.

Blenkinsop, T.G. *Deformation Microstructures and Mechanisms in Minerals and Rocks.* Kluwer, Dordrecht, 2000.

Boozer, G.D., Hiller, K.H., and Serdengecti, S. Effects of pore fluids on the deformation behaviour or rocks subjected to triaxial compression. In *Rock Mechanics. Fifth Symp. Rock Mechanics.* Fairhurst, C., ed., pp. 579–624, Pergamon Press, Oxford, 1963.

Boutéca, M., Sarda, J.-P., and Schneider, F. Subsidence induced by the production of fluids. *Rev. Inst. Franc. Petr.* 51: 349–379, 1996.

Brace, W.F., and Riley, D.K. Static uniaxial deformation of 15 rocks to 30 kb. *Int. J. Rock Mech. Min. Sci.* 9: 271–288, 1972.

Brace, W.F., Silver, E., Hadley, K., and Goetze, C. Cracks and pores—A close look. *Science* 178: 163–165, 1972.

Brandt, H. A study of the speed of sound in porous granular media. *J. Appl. Mech.* 22: 479–486, 1955.

Bray, C.J., and Karig, D.E. Porosity of sediments in accretionary prisms and some implications for dewatering processes. *J. Geophys. Res.* 90: 768–778, 1985.

Briggs, A. *Acoustic Microscopy.* Clarendon Press, Oxford, 1992.

Byerlee, J. Friction, overpressure and fault normal compression. *Geophys. Res. Let.* 17: 2109–2112, 1990.

Byrne, T., Maltman, A., Stephenson, E., Soh, W., and Knipe, R. Deformation structures and fluid flow in the toe region of the Nankai accretionary prism. *Proc. of the ODP, Scientific Results.* 131: 83–192, 1993.

Caruso, L., Simmons, G., and Wilkens, R. The physical properties of a set of sandstones—Part I. The samples. *Int. J. Rock Mech. Min. Sci.* 22: 381–392, 1985.

Chen, W.F. Soil mechanics, plasticity and landslides. In *Mechanics of Inelastic Materials*, Dvorak, G.J., and Shield, R.T., eds., pp. 31–58. Elsevier, Amsterdam, 1984.

Chester, F.M., and Logan, J.M. Implications for mechanical properties of brittle faults from observations of the Punchbowl fault zone, California. *Pure Appl. Geophys.* 124: 79–196, 1986.

Choquette, P.W., and James, N.P. Diagenesis in limestones—the deep burial environment. *Geosciences Canada* 14: 3–35, 1986.

Coker, D.A., Torquato, S., and Dunsmuir, J.H. Morphology and physical properties of Fontainebleau sandstone via tomographic analysis. *J. Geophys. Res.* 101: 17497–17506, 1996.

Coles, M.E. X-ray imaging. In *Experimental Methods in the Physical Sciences.* Wong, P.-Z., ed. vol. 35, pp. 301–336. Academic Press, San Diego, 1999.

Cundall, P.A. A computer model for simulating progressive, large-scale movements in blocky rock systems. In *Proc. Symp. Int. Soc. Rock Mech.,* p. 8. Nancy, France 1971.

Curran, J.H., and Carroll, M.M. Shear stress enhancement of void compaction. *J. Geophys. Res.* 84: 1105–1112, 1979.

Danburg, J.S., and Yuhas, D.E. Acoustic microscope images of rock samples. *Geophys. Res. Lett.* 5: 885–888, 1978.

Darot, M., and Reuschlé, T. Direct assessment of Wood's metal wettability on quartz. *Pure Appl. Geophys.* 155: 119–129, 1999.

David, C., Wong, T.-f., Zhu, W., and Zhang, J. Laboratory measurement of compaction-induced permeability change in porous rock: Implications for the generation and maintenance of pore pressure excess in the crust. *Pure Appl. Geophys.* 143: 425–456, 1994.

David, C., Menéndez, B., and Bernabé, Y. The mechanical behaviour of synthetic sandstone with varying brittle cement content. *Int. J. Rock Mech. Min. Sci.* 35: 759–770, 1998.

Davies, P.B. Evaluation of the role of threshold pressure in controlling flow of waste-generated gas into bedded salt at the Waste Isolation Pilot Plant. Sandia National Laboratories, Albuquerque, NM, 1991.

den Brok, S.W.J., David, C., and Bernabé, Y. Preparation of synthetic sandstones with variable cementation for studying the physical properties of granular rocks. *C. R. Acad. Sci.* 325: 487–492, 1997.

Desai, C.S., and Siriwardane, H.J. *Constitutive Laws for Engineering Materials*. Prentice-Hall, Englewood Cliffs, NJ, 1984.

DiGiovanni, A.A., Fredrich, J.T., Holcomb, D.J., and Olsson, W.A. Micromechanics of compaction in an analogue reservoir sandstone. *In Proc. Fourth North Am. Rock Mech. Symp.,* pp. 1153–1160. A.A. Balkema, Rotterdam, The Netherlands, 2000.

DiMaggio, F.L., and Sandler, I.S. Material model for granular soils. *J. Eng. Mech. Div., ASCE* 97: 935–950, 1971.

Doser, D.I., Baker, M.R., and Mason, D.B. Seismicity in the War-Wink gas field, Delaware Basin, West Texas, and its relationship to petroleum production. *Bull. Seism. Soc. Am.* 81: 971–986, 1991.

Domenico, P.A., and Schwartz, F.W. *Physical and Chemical Hydrogeology*, 2nd ed. John Wiley, New York, 1998.

Dullien, F.A.L., and Dhawan, G.K. Bivariate pore-size distribution of some sandstones. *J. Coll. Interface Sci.* 52: 129–135, 1975.

Dvorkin, J., Mavko, G., and Nur, A. The effect of cementation on the elastic properties of granular materials. *Mech. Mat.* 12: 207–217, 1991.

Dvorkin, J., Nur, A., and Yin, H. Effective properties of cemented granular cemented materials. *Mech. Mat.* 18: 351–366, 1994.

El Bied, A., Sulem, J., and Martineau, F. Microstructure of shear zones in Fontainebleau sandstone. *Int. J. Rock Mech. Min. Sci.* 39: 917–932, 2002.

Elliott, G.M., and Brown, E.T. Yield of a soft, high porosity rock. *Geotechnique* 35: 413–423, 1985.

Fatt, I. Compressibility of sandstones at low to moderate pressures. *Bull. Am. Asso. Petrol. Geol.* 42: 1924–1957, 1958.

Fisher, Q.J., Casey, M., Clennell, M.B., and Knipe, R.J. Mechanical compaction of deeply buried sandstones of the North Sea. *Mar. Petrol. Geol.* 16: 605–618, 1999.

Flannery, B.P., Deckman, H.W., Roberge, W.G., and D'Amico, K.L. Three dimensional x-ray microtomography. *Science* 237: 1439–1444, 1987.

Fowles, J., and Burley, S. Textural and permeability characteristics of faulted, high porosity sandstones. *Mar. Petrol. Geol.* 11: 608–623, 1994.

Fredrich, J.T. 3-Dimensional imaging of porous media using laser scanning confocal microscopy with application to microscale transport processes. *Phys. Chem. Earth (A)* 24: 551–561, 1999.

Fredrich, J.T., Deitrick, G.L., Arguello, J.G., and deRouffignac, E.P. Geomechanical modeling of reservoir compaction, surface subsidence, and casing damage at the Belridge diatomite field. *SPE Res. Eval. Eng.* 3: 348–359, 2000.

Fredrich, J.T., Menendez, B., and Wong, T.-f. Imaging the pore structure of geomaterials. *Science,* 268: 276–279, 1995.

Fukushima, E. Nuclear magnetic resonance as a tool to study flow. *Annu. Rev. Fluid Mech.* 31: 95–123, 1999.

Geertsma, J. Land subsidence above compacting oil and gas reservoirs. *J. Pet. Tech*., 25, 734–744, 1973.

Géraud, Y., Caron, J.-M., and Faure, P. Porosity network of a ductile shear zone. *J. Struct. Geol.* 17: 1757–1769, 1995.

Goldsmith, A.S. Permeability decline and compressibility in sandstone reservoir rocks. In *Rock at Great Depth*, Maury, V., and Fourmaintraux, D., eds., pp. 923–928, A. A. Balkema, Rotterdam, The Netherlands, 1989.

Grasso, J.R., and Wittlinger, G. Ten years of seismic monitoring over a gas field area. *Bull. Seism. Soc. Am.* 80: 450–473, 1990.

Gratier, J.-P., Renard, F., and Labaume, P. How pressure solution creep and fracturing processes interact in the upper crust to make it behave in both a brittle and viscous manner. *J. Struct. Geol.* 21: 1189–1197, 1999.

Griffith, A.A. The phenomena of rupture and flow in solids. *Phil. Trans. Roy. Soc.* A221: 163–198, 1920.

Griggs, D.T., Turner, F.J., and Heard, H.C. Deformation of rocks at 500° to 800°C. In *Rock Deformation, GSA Memoir 79*, Griggs, D., and Handin, J., eds., pp. 39–104. Geological Society of America, 1960.

Guéguen, Y., and Palciauskas, V. *Introduction to the Physics of Rocks.* Princeton University Press, Princeton, 1994.

Hadizadeh, J., and Law, R.D. Water-weakening of sandstone and quartzite deformed at various stress and strain rates. *Int. J. Rock Mech. Min. Sci.* 28: 431–439, 1991.

Hamilton, G.M., and Goodman, L.E. The stress field created by a circular sliding contact. *J. Appl. Mech.* 33: 371–376, 1966.

Hazzard, J.F., Young, R.P., and Maxwell, S.C. Micromechanical modeling of cracking and failure in brittle rocks. *J. Geophys. Res.* 105: 16683–16697, 2000.

Hiemstra, J.F., and van der Meer, J.J.M. Pore-water controlled grain fracturing as an indicator for subglacial shearing in tills. *J. Glaciol.* 43: 446–454, 1997.

Holt, R.M. Particle vs. laboratory modelling of in situ compaction. *Phys. Chem. Earth* A 26: 89–93, 2001.

Homand, S., and Shao, J.F. Mechanical behaviour of a porous chalk and effect of saturating fluid. *Mech. Cohes.-Frict. Mater.* 5: 583–606, 2000.

Irwin, G.R. Fracture. In *Handbuck der Physik*, Flugge, S. ed. Springer-Verlag, Berlin, 1958.

Jeng, F.-S., Weng, M.-C., Hunag, T.-H., and Lin, M.-L. Deformational characteristics of weak sandtone and impact to tunnel deformation. *Tunnel. Undergr. Space Tech.* 17: 263–274, 2002.

Jones, M.E., and Leddra, M.J. Compaction and flow of porous rocks at depth. In *Rock at Great Depth*, Maury, V., and Fourmaintraux, D., eds., pp. 891–898, A. A. Balkema, Rotterdam, The Netherlands, 1989.

Kawakata, H., Cho, A., Kiyama, T., Yanagidani, T., Kusunose, K., and Shimada, M. Three dimensional observations of faulting process in Westerly granite under uniaxial and triaxial conditions by X-ray CT scan. *Tectonophysics* 313: 293–305, 1999.

Kenyon, W.E. Nuclear magnetic resonance as a petrophysical measurement. *Nuclear Geophys.* 6: 153–171, 1992.

Kirby, S.H., Durham, W.B., and Stern, L. The ice I->II transformation: Mechanisms and kinetics under hydrostatic and nonhydrostatic conditions. In *Physics and Chemistry of Ice*, Maeno, N., and Hondoh, T., eds., pp. 456–463, Hokkaido University Press, Sapporo, 1992.

Klein, E., Baud, P., Reuschlé, T., and Wong, T.-f. Mechanical behaviour and failure mode of Bentheim sandstone under triaxial compression. *Phys. Chem. Earth* A 26: 21–25, 2001.

Kleinberg, R.L. Nuclear magnetic resonance. In *Experimental Methods in the Physical Sciences*, Wong, P.-Z., ed. vol. 35, pp. 337–385, Academic Press, San Diego, 1999.

Koplik, J., Lin, C., and Vermette, M. Conductivity and permeability from microgeometry. *J. Appl. Phys.* 56: 3127–3131, 1984.

Kranz, R.L. Microcracks in rocks, a review. Tectonophysics 100: 449–480, 1983.

Lajtai, E.Z., Schmidtke, R.H., and Bielus, L.P. The effect of water on the time-dependent deformation and fracture of granite. *Int. J. Rock Mech. Min. Sci.* 24: 247–255, 1987.

Lambe, T.W., and Whitman, R.V. *Soil Mechanics*. John Wiley, New York, 1969.

Laubach, S.E. A method to detect natural fracture strike in sandstones. *AAPG Bull.* 81: 604–623, 1997.

Lawn, B. *Fracture of Brittle Solids*, 2nd ed. Cambridge University Press, Cambridge, 1993.

Lawn, B.R. Indentation of ceramics with spheres: A century after Hertz. *J. Am. Ceram. Soc.* 81: 1977–1994, 1998.

Lindquist, W.B., Venkatarangan, A., Dunsmuir, J., and Wong, T.-f. Pore and throat size distributions measured from synchrotron X-ray tomographic images of Fontainebleau sandstones. *J. Geophys. Res.* 105: 21509–21527, 2000.

Lloyd, G.E., and Hall, M.G. Application of scanning electron microscopy to the study of deformed rocks. *Tectonophysics* 78: 687–698, 1981.

Mair, K., Main, I.G., and Elphick, S.C. Sequential development of deformation bands in the laboratory. *J. Struct. Geol.* 22: 25–42, 2000.

Makse, H.A., Johnson, D.L., and Schwartz, L. Force fluctuations in unconsolidated granular materials under uniaxial compression. *Phys. Rev. Lett.* 84: 4160–4163, 2000.

Mavko, G., Mukerji, T., and Dvorkin, J. *The Rock Physics Handbook: Tools for Seismic Analysis in Porous Media.* Cambridge University Press. Cambridge, 1998.

McEwen, T.J. Brittle deformation in pitted pebble conglomerates. *J. Struct. Geol.* 5: 25–37, 1981.

Menéndez, B., Zhu, W., and Wong, T.-f. Micromechanics of brittle faulting and cataclastic flow in Berea sandstone. *J. Struct. Geol.* 18: 1–16, 1996.

Menéndez, B., David, C., and Nistal, A.M. Confocal scanning laser miroscopy applied to the study of pore and crack networks in rocks. Computers & Geosciences 27: 1101–1109, 2001.

Mindlin, R.D. Compliance of elastic bodies in contact. *J. Appl. Mech.,* ASME 16: 259–268, 1949.

Mollema, P.N., and Antonellini, M.A. Compaction bands: A structural analog for anti-mode I cracks in aeolian sandstone. *Tectonophysics* 267: 209–228, 1996.

Montoto, M., Martinez-Nistal, A., Rodriguez-Rey, A., Fernandez-Merayo, N., and Soriano, P. Microfractography of granitic rocks under confocal scanning laser microscopy. *J. Micros.* 177: 138–149, 1995.

Morgenstern, N.R., and Phukan, A.L.T. Non-linear stress-strain relations for a homogeneous sandstone. *Int. J. Rock Mech. Min. Sci.* 6: 127–142, 1969.

Myer, L.R., Kemeny, J., Cook, N.G.W., Ewy, R., Suarez, R., and Zheng, Z. Extensile cracking in porous rock under differential compressive stress. *Appl. Mech. Rev.* 45: 263–280, 1992.

Nagel, N.B. Compaction and subsidence issues within the petroleum industry: From Wilmington to Ekofisk and beyond. *Phys. Chem. Earth* A 26: 3–14, 2001.

Olsson, W.A., and Holcomb, D.J. Compaction localization in porous rock. *Geophys. Res. Lett.* 27: 3537–3540, 2000.

Orowan, E. The fatigue of glass under stress. *Nature* 154: 341–343, 1944.

Osment, P.A., Packer, K.J., Taylor, M.J., Attard, J.J., Carpenter, T.A., Hall, L.D., Herrod, N.J., and Doran, S.J. NMR imaging of fluids in porous solids. *Phil. Trans. R. Soc. Lond*. A 333: 441–452, 1990.

Papka, S.D., and Kyriakides, S. Biaxial crushing of honeycombs—Part I: Experiments. *Int. J. Solids Struct.* 36: 4367– 4396, 1999.

Paterson, M.S. The ductility of rocks. In *Physics of Strength and Plasticity*, ed., Argon, A.S., pp. 377–392. MIT Press, Cambridge, MA, 1969.

Paterson, M.S. Deformation mechanisms in carbonate crystals. In *Physis of Materials, A Festschrift for Dr. Walter Boas*, eds., Borland, D.W., Clarebrough, L.M., and Moore, A.J.W., pp. 199–208, CSIRO and Department of Metallurgy, University of Melbourne, Victoria, 1979.

Paterson, M.S. *Experimental Rock Deformation—The Brittle Field*. Spinger-Verlag, New York, 1978.

Petford, N., Davidson, G., and Miller, J.A. Pore structure determination using confocal scanning laser microscopy. *Phys. Chem. Earth* A 24: 563–567, 1999.

Pettijohn, F.J. *Sedimentary Rocks*, 3rd ed. Harper & Row, New York, 1975.

Pissarenko, D., and Gland, N. Modeling of scale effects of damage in cemented granular rocks. *Phys. Chem. Earth* A 26: 83–88, 2001.

Pittman, E.D., and Duschatko, R.W. Use of pore casts and scanning electron microscopy to study pore geometry. *J. Sed. Petr.* 40: 1153–1157, 1970.

Pittman, E.D. The pore geometries of reservoir rocks. In *Physics and Chemistry of Porous Media*, Johnson, D.C., and Sen, P.N., eds., pp. 1–19, AIP Conference Proceedings 107, New York, 1984.

Raynaud, S., Fabre, D., Mazerolle, F., Géraud, Y., and Latière, H.J. Analysis of the internal structure of rocks and characterization of mechanical deformation by a non-destructive method: X-ray tomodensitometry. *Tectonophysics* 159: 149–159, 1989.

Rehbinder, P.A., Schreiner, L.A., and Zhigach, K.F. Hardness reducers in drilling. Melbourne: Council for Scientific and Ind. Res. (78), 1948.

Rhett, D.W., and Teufel, L.W. Stress path dependence of matrix permeability of North Sea sandstone reservoir rock. *Proc. U. S. Symp. Rock Mechanics* 33: 345–354, 1992.

Risnes, R., Kristensen, C.N., and Andersen, M.A. Triaxial tests on high porosity chalk with different saturating fluids. In *Fifth North Sea Chalk Symposium*, p. 12. Reims, France, 1996.

Rodriguez-Rey, A., Briggs, G.A.D., Field, T.A., and Montoto, M. Acoustic microscopy of rock. *J. Microsc.* 160: 21–29, 1990.

Russ, J.C. *Practical Stereology.* Plenum, NewYork, 1986.

Rutter, E.H. The influence of interstitial water on the rheological behavior of calcite rocks. *Tectonophysics* 14: 13–33, 1972.

Rutter, E.H. The influence of temperature, strain rate and interstitial water in the experimental deformation of calcitic rocks. *Tectonophysics* 22: 311–334, 1974.

Schmitt, L., Forsans, T., and Santarelli, F. Shale testing and capillary phenomena. *Int. J. Rock Mech. Min. Sci.* 31: 411–427, 1994.

Schofield, A.N., and Wroth, C.P. *Critical State Soil Mechanics*. McGraw Hill, New York, 1968.

Schroeder, C., Bois, A.P., Maury, V., and Hallé, G. Water/chalk (or collapsible soil) interaction: Part III—Results of tests performed in laboratory on Lixhe chalk to calibrate water/chalk models. *Proc. Eurock'98*, SPE/ISRM 47587, 2: 505–514, 1998.

Schulson, E.M., and Nickolayev, O.Y. Failure of columnar saline ice under biaxial compression: Failure envelopes and the brittle-ductile transition. *J. Geophys. Res.* 100: 22383–22400, 1995.

Schutjens, P.M.T.M., and de Ruig, H. The influence of stress path on compressibility and permeability of an overpressurised reservoir sandstone: Some experimental data. *Phys. Chem. Earth* 22: 97–103, 1997.

Segall, P. Earthquakes triggered by fluid extraction. Geology 17: 942–946, 1989.

Segall, P., and Fitzgerald, S.D. A note on induced stress changes in hydrocarbon and geothermal reservoirs. *Tectonophysics* 289: 117–128, 1998.

Shah, K.R., and Wong, T.-f. Fracturing at contact surfaces subjected to normal and tangential loads. *Int. J. Rock Mech. Min. Sci.* 34: 722–739, 1997.

Sibson, R.H. Crustal stress, faulting and fluid flow. In *Geofluids: Origins, Migration and Evolution of Fluids in Sedimentary Basins,* Parnell, J., ed., pp. 69–84. Geological Society Special Publication, London, 1994.

Shipton, Z.K., and Cowie, P.A. Damage zone and slip-surface evolution over mm to km scales in high-porosity Navajo sandstone, Utah. *J. Struct. Geol.* 23: 1825–1844, 2001.

Smits, R.M.M., de Waal, J.A., and van Kooten, J.F.C. Prediction of abrupt reservoir compation and surface subsidence caused by pore collapse in carbonates. SPE Form. Eval., 340–346, 1988.

Snoke, A.W., Tullis, J., and Todd, V.R. *Fault-related Rocks, A Photographic Atlas*. Princeton University Press, Princeton, 1998.

Spanne, P., Thovert, J.F., Jacquin, C.J., Lindquist, W.B., Jones, K.W., and Adler, P.M. Synchrotron computer microtomography of porous media: Topology and transports. *Phys. Rev. Lett.* 73: 2001–2004, 1994.

Suarez-Rivera, F.R., Cook, N.G.W., Cooper, G.A., and Zheng, Z. Indentation by pore collapse in porous rocks. In *Rock Mechanics Contributions and Challenges, Proceedings of the Thirty first U.S. Symposium on Rock Mechanics*, Hustrulid, W.A., and Johnson, G.A., eds., pp. 653–660, A. A. Balkema, Rotterdam, The Netherlands, 1990.

Teufel, L.W., Rhett, D.W., and Farrell, H.E. Effect of reservoir depletion and pore pressure drawdown on in situ stress and deformation in the Ekofisk field, North Sea. In *Proc. U. S. Rock Mechanics Symp*., 32, 63–72, 1991.

Thiercelin, M. Parameters controlling rock indentation. In *Rock at Great Depth*, Maury, V., and Fourmaintraux, D., eds., pp. 85–92. A. A. Balkema, Rotterdam, The Netherlands, 1989.

Turner, F.J., Griggs, D.T., and Heard, H.C. Experimental deformation of calcite crystals. *Geol. Soc. Am. Bull.* 65: 883–954, 1954.

Underwood, E.E. *Quantitative Stereology*. Addison Wesley, Reading, 1970.

Vajdova, V., Baud, P., and Wong, T.-f. Compaction, dilatancy and failure in porous carbonate rocks. *J. Geophys. Res*., in press.

Van der Meer, J.J.M. Microscopic evidence of subglacial deformation. *Quart. Sci. Rev.* 12: 553–587, 1993.

Walsh, J.B. The effect of cracks on the compressibility of rocks. *J. Geophys. Res.* 70: 381–389, 1965.

Wardlaw, N.C. Pore geometry of carbonate rocks as revealed by pore casts and capillary pressure. *Am. Asso. Petrol. Geol. Bullet.* 60: 245–257, 1976.

Wawersik, W.R., Rudnicki, J.W., Dove, P., Harris, J., Logan, J.M., Pyrak-Nolte, L., Orr, F.M., Ortoleva, P., Richter, J.F., Warpinski, N.R., Wilson, J.L., and Wong, T.-f. Terrestrial sequestration of CO2: An assessment of research needs. *Advances in Geophysics* 43: 97–177, 2000.

Wellington, S.L., and Vinegar, H.J. X-ray computerized tomography. *J. Pet. Tech.* 39: 885–898, 1987.

Willemse, E.J.M., Peacock, D.C.P., and Aydin, A. Nucleation and growth of strike-slip faults in limestones from Somerset, U.K. *J. Struct. Geol.* 19: 1461–1477, 1997.

Wong, T.-f., Szeto, H., and Zhang, J. Effect of loading path and porosity on the failure mode of porous rocks. *Appl. Mech. Rev.* 45: 281–293, 1992.

Wong, T.-f., and Wu, L.-C. Tensile stress concentration and compressive failure in cemented granular material. *Geophys. Res. Let.* 22: 1649–1652, 1995.

Wong, T.-f., David, C., and Zhu, W. The transition from brittle faulting to cataclastic flow in porous sandstones: Mechanical deformation. *J. Geophys. Res.* 102: 3009–3025, 1997.

Wong, T.-f., and Baud, P. Mechanical compaction of porous sandstone. Oil & Gas Science and Technology—Rev. IFP, 54, 715–727, 1999.

Wong, T.-f., Baud, P., and Klein, E. Localized failure modes in a compactant porous rock. *Geophys. Res. Lett.* 28: 2521–2524, 2001.

Wu, X.Y., Baud, P., and Wong, T.-f. Micromechanics of compressive failure and spatial evolution of anisotropic damage in Darley Dale sandstone. *Int. J. Rock Mech. Min. Sci.* 37: 143–160, 2000.

Yin, H., and Dvorkin, J. Strength of cemented grains. *Geophys. Res. Lett.* 21: 903–906, 1994.

Yu, P., Mustata, M., Chen, D., Pyrak-Nolte, L.J., and Nolte, D.D. Holographic 3-Dimensional laser imaging into sandstone. *Geophys. Res. Lett.* 29 (20): 49–1–49-4, 2002.

Zhang, J., Wong, T.-f., and Davis, D.M. Micromechanics of pressure-induced grain crushing in porous rocks. *J. Geophys. Res.* 95: 341–352, 1990a.

Zhang, J., Wong, T.-f., Yanagidani, T., and Davis, D.M. Pressure-induced microcracking and grain crushing in Berea and Boise sandstones: Acoustic emission and quantitative microscopy measurements. *Mech. Mater.* 9: 1–15, 1990b.

Zimmerman, R.W. The Effect of Pore Structure on the Pore and Bulk Compressibilities of Consolidated Sandstones. Ph.D. diss. University of California at Berkeley, 1984.

Zimmerman, R.W. *Compressibility of Sandstones*. Elsevier, Amsterdam, 1991.

Zhu, W., and Wong, T.-f. The transition from brittle faulting to cataclastic flow: Permeability evolution. *J. Geophys. Res.* 102: 3027–3041, 1997.